INFLUENCE OF THE CALCINATION TEMPERATURE ON THE ACTIVITY OF HYDROXYAPATITE-SUPPORTED PALLADIUM CATALYST IN THE METHANE OXIDATION REACTION

Z. Boukha, A. Choya, M. Cortés-Reyes, B. de Rivas, L.J. Alemany, J.R. González-Velasco, J.I. Gutiérrez-Ortiz, R. López-Fonseca

Applied Catalysis B: Environmental 277 (2020) 119280

DOI: 10.1016/j.apcatb.2020.119280

INFLUENCE OF THE CALCINATION TEMPERATURE ON THE ACTIVITY OF HYDROXYAPATITE-SUPPORTED PALLADIUM CATALYST IN THE METHANE OXIDATION REACTION

Zouhair Boukha[(a)], Andoni Choya[(a)], Marina Cortés-Reyes[(b)], Beatriz de Rivas[(a)], Luis J. Alemany[(b)], Juan R. González-Velasco[(a)], José I. Gutiérrez-Ortiz[(a)], Rubén López-Fonseca[(a)]

(a) Chemical Technologies for Environmental Sustainability Group, Department of Chemical Engineering, Faculty of Science and Technology, University of the Basque Country UPV/EHU, P.O. Box 644, E-48080 Bilbao, Spain.
(b) Department of Chemical Engineering, Faculty of Sciences, , Campus de Teatinos, University of Málaga, Málaga, E-29071, Spain.

*Corresponding author: Zouhair Boukha

Phone: +34 946015502

Fax: +34 946013500

E-mail address: zouhair.boukha@ehu.eus

Abstract

In the present study, a series of four hydroxyapatite (HAP) supported palladium samples, with a Pd loading close to 0.5%, obtained through their calcination at 773, 873, 973, or 1073 K has been investigated. These samples have been characterized using a wide battery of complementary techniques. From these studies, it was found that the rise of the calcination temperature induces a progressive dehydroxylation of the support and a structure evolution of the species containing Pd^{2+}, from tetrahedral (Td) to square planar geometry (D_{4h}). Moreover, this enhances markedly the metal-support interactions. For instance, at the highest temperature (1073 K), Pd particles were found encapsulated by a thin support layer. Consequently, two distinct reducible species have been identified; one of them manifests SMSI. This increase in the Pd-HAP interaction strength seems to (i) expand the HAP lattice, (ii) change the Pd^{2+} coordination from Td to D_{4h} geometry, (iii) promote PdO reduction and (iv) suppress CO chemisorption. These entire properties do compensate the poor textural properties and benefit the efficiency and stability of the Pd active phase in methane oxidation reaction.

Keywords: Palladium-supported hydroxyapatite; calcination temperature; structural evolution; methane oxidation reaction; Pd active species; effect of water addition.

1. Introduction

Natural gas presents an important alternative for the replacement and diversification of conventional energy sources. Due to its high calorific value (46-56 kJ g^{-1}), it is largely used in heat generators in a variety of applications [1-5]. However, its direct combustion generates pollutants harmful to the environment. In this sense, it is well known that the emission of unburned methane presents a serious problem contributing to the greenhouse effect. This is because, though it is less abundant in the atmosphere, methane is much more active than CO_2.

Palladium-based catalysts have been widely used in the catalytic oxidation of methane because of their high specific activity [1-12]. According to previous studies, the PdO phase is highly active at low temperatures (≤ 823 K). Others authors have claimed that the most active phase is composed of Pd/PdO interfaces that generate a high oxygen mobility [1,2]. Baylet et al. [10] reported that the re-oxidation of large Pd^o particles, dispersed on alumina support, starts at 573 K and needs high temperatures (> 823 K) to get completely oxidized. Under lean methane combustion conditions, they observed that the surface PdO species were partially reduced while the bulk PdO kept its oxidation state unchanged. The observed changes in the redox properties of the active phase are accompanied by an oscillatory behavior of the catalytic activity. As a matter of fact, generally, activity hysteresis has been observed on various Pd catalysts submitted to successive cycles of temperature [1,12].

Though alumina is by far the most commonly used, current research is dedicated to the synthesis of alternative catalyst supports exhibiting suitable properties in order to overcome the main problems leading to deactivation of Pd catalysts, namely sintering and the undesirable changes in the oxidation state of palladium [1,4-14]. Furthermore, the Pd catalysts should be able to withstand the water inhibition effect which might

accelerate their deactivation process. Despite there is still no wide consensus on the intrinsic deactivation mechanism by water, the most proposed one consists of the formation of surface hydroxyl groups that block the active sites and/or limit the re-oxidation of Pd [4,5].

On the other hand, it is well known that the thermal treatment of the Pd catalysts is a key factor influencing the oxidation state of the active phase and its interaction with the support [3,8,12]. Yashnik et al. [12] studied the effect of the calcination temperature (773-1473 K) on the activity of a Pd/$MnLaAl_{11}O_{19}$ catalyst. They found a positive effect on the hysteresis curves over the samples calcined at a temperature higher than 1023 K. This behavior was assigned to the formation of highly dispersed PdO spread on the surface of metallic Pd in the form of a polycrystalline film or small domains.

Hydroxyapatite material has attracted considerable attention in the field of heterogeneous catalysis, being used as catalyst support for numerous applications [1,15-26]. In their study on a Pd/HAP system, Tang et al. [26] reported that it provides oxidative strong metal-support interactions (OMSI) at high temperatures owing to the loss of surface OH groups. Moreover, the resulting encapsulated Pd species showed a high catalytic stability when submitted to 4 cycles of the Suzuki cross-coupling reaction. In a comparative study dealing with the methane oxidation activity over Pd loaded hydroxyapatite and fluoroapatite (FAP) materials, it was found that Pd/HAP was remarkably more active than Pd/FAP catalyst [1]. The low activity of the latter was related to the presence of surface fluor species which favored the reduction of PdO in the methane-air mixture and prevented their re-oxidation as required by the redox process.

The major objective of this work is to investigate the catalytic properties of a series of HAP-supported palladium samples for the combustion of lean methane. A special

attention has been paid to analyzing the influence of the calcination temperature in the 773-1073 K range on the properties of the Pd/HAP samples, characterized using BET, XRD, XPS, UV-Visible-NIR, H_2-TPR, CH_4-TPR, H_2 chemisorption, TEM, OSC, NH_3-TPD, CO_2-TPD and FTIR techniques. The above-mentioned studies have allowed us to determine the optimum thermal treatment and to correlate the activity of the Pd/HAP samples with their structural and chemical features.

2. Experimental

Calcium-deficient hydroxyapatite support was synthesized by precipitation method, adding drop wise a calcium nitrate solution (Merck) to a solution of $(NH_4)_2HPO_4$ (Sigma-Aldrich). The pH of the precipitation was adjusted to 10, by adding ammonia solution. The mixture was then stirred at 353 K for 16 h. After filtration, the recovered solid was washed with distilled water, dried overnight at 393 K and finally calcined in air at 773 K for 4 h.

The Pd/HAP catalyst (with a Pd loading of 0.5 wt.%) was prepared by incipient wetness impregnation of the synthesized support from an aqueous solution of tetraammine palladium (II) chloride monohydrate (Sigma-Aldrich). The impregnated sample was dried overnight at 393 K and, then, separated in four portions, which were calcined for 4 h at various temperatures (T_c), namely 773, 873, 973 and 1073 K.

The textural properties of the catalysts were determined by N_2 physisorption experiments at 77 K on a Micromeritics (TRISTAR II 3020) apparatus. Before their analysis, the samples were evacuated at 573 K under nitrogen flow for 8 h.

The structural properties of the bare supports and the Pd catalysts were investigated by X-ray diffraction (XRD). The analyses were conducted on a X'PERT-MPD X-ray diffractometer with Cu Kα radiation (λ = 1.5406 Å). The HAP lattice parameters were

estimated including the whole XRD diffractogram. For this full profile refinement, the unit-cell parameters, peak shape (pseudo-Voigt), background, systematic 2θ shift, U, V, W half-width parameters for the profile function, and asymmetry parameters were evaluated. The degree of crystallinity (X_c) of the HAP support was estimated using the following expression [27]:

$$X_c = 1 - \frac{V_{112/300}}{I_{300}} \quad (1)$$

where $V_{112/300}$ is the intensity of the hollow between the peaks corresponding to (112) and (300) reticular planes and I_{300} is the intensity of the (300) reflection.

The coordination of the Pd species was investigated by diffuse reflectance UV-vis-NIR spectroscopy (UV-vis-NIR DRS) with a Cary 5000 apparatus. The spectra were recorded at room temperature in the range of 200-2500 nm.

The X-ray photoelectron spectroscopy (XPS) analyses were performed on a PHI-5701 spectrometer, equipped with a X-ray source operating with Mg and Al anodes, PHI 04-548 model.

The morphology, mean size and the dispersion of the Pd particles, spread on the samples reduced at 473 K, were investigated by Transmission Electron Microscopy (TEM). These analyses were performed using a Philips CM200 microscope, operating at 200 kV, and equipped with LaB6 filament. The mean inter-particle distance (X_i) was estimated according to the following expression [28]:

$$X_i = \sqrt{\frac{\pi \sigma d^3 S_{BET}\,(100 - y)}{3\sqrt{3}\,y}} \quad (2)$$

where σ, d, S_{BET} and y represent the density of Pd particles (g nm^{-3}), mean diameter of Pd particles (nm), specific surface area (nm^2 g^{-1}) and Pd loading, respectively.

The Pd dispersion was also estimated by H_2 chemisorption at 353 K using an AutoChem 2920 instrument. The samples were pre-reduced flowing 5%H_2/Ar (50 cm^3 min^{-1}) at 473 K for 2 h. Thereafter, they were purged under Ar flow (50 cm^3 min^{-1}) at 773 K for 1 h and, then, cooled to 353 K. Finally, the H_2 pulses (5%H_2/Ar, loop volume: 0.5 cm^3) were injected in Ar carrier (50 cm^3 min^{-1}) over the sample, at 353 K. The Pd dispersion, defined as the exposed active metal fraction, was determined on the assumption of a unity adsorption stoichiometry ($H/Pd_s = 1$) where "Pd_s" stands for the surface Pd atoms.

Temperature-programmed reduction (H_2-TPR) experiments were conducted on a Micromeritics AutoChem 2920 instrument coupled to a mass spectrometer (MKS Cirrus LM99). The samples were pre-treated in a flow of 5%O_2/He at 773 K for 30 min and then cooled down to 243 K in He. Then, they were reduced under a 5%H_2/Ar flow (50 cm^3 min^{-1}) raising the temperature from 243 to 773 K with a ramp of 10 K min^{-1}.

The reducibility of the catalysts was also investigated by methane temperature-programmed reduction (CH_4-TPR) using the same experimental procedure as for H_2-TPR experiments. The reduction step was conducted using a 5%CH_4/He flow (50 cm^3 min^{-1}) raising the temperature from 373 to 960 K with a ramp of 10 K min^{-1}. In this case, CH_4 (*m/z*:15), CO_2 (*m/z*:44), H_2 (*m/z*:2) and CO (m/z:28) signals were monitored using a mass spectrometer (MKS Cirrus LM99).

The FTIR study of CO adsorption was carried out with a CARRY 600 series FTIR apparatus. The samples consisting of self-supported disks were introduced in a high temperature cell equipped with ZnSe windows (Specac). Prior to the adsorption period, the samples were reduced in-situ at 473 K, for 1 h, under 5%H_2/Ar flow (200 cm^3 min^{-1}) and evacuated at 523 K, for 1 h, under Ar flow. After a subsequent evacuation in Ar at 303 K (30 min), the background spectrum was recorded averaging 52 scans with a

resolution of 4 cm^{-1}. Then, the adsorption and desorption spectra were recorded after exposure to 750 ppm CO (diluted in Ar) at 303 K (45 min) followed by evacuation under Ar (45 min), respectively.

The ultimate Oxygen Storage Capacity (OSC) was evaluated by means of oxygen volumetric chemisorption experiments performed at 623, 673, 723 and 773 K, respectively, on a Micromeritics AutoChem 2920 instrument. The samples (100 mg) were pre-reduced in a flow of 5%H_2/Ar (50 cm^3 min^{-1}) at 773 K for 1 h and, then, evacuated (under He) at 773 K for 1 h. Finally, after their cooling to the selected analysis temperature, the samples were submitted to twenty O_2 pulses (5%O_2/He, loop volume: 0.5 cm^3), injected in He carrier (50 cm^3 min^{-1}).

The temperature programmed desorption of CO_2 (CO_2-TPD) experiments were performed on a Micromeritics AutoChem 2920 apparatus coupled to a mass spectrometer (MKS Cirrus LM99). The samples were pre-treated at 773 K (30 min) in a flow 5%O_2/He (50 cm^3 min^{-1}) and cooled to 323 K under He. The adsorption of CO_2 was performed in a flow of 5%CO_2/He (50 cm^3 min^{-1}) for 30 min. After CO_2 adsorption the samples were treated with He for 2 h and heated at 10 K min^{-1} up to 773 K in flowing He (50 cm^3 min^{-1}). The acid properties of the samples were investigated by temperature programmed desorption of NH_3 (NH_3-TPD). The samples were submitted to the same experimental procedures used for CO_2-TPD. The gas stream was 50 cm^3 min^{-1} of 5%NH_3/He.

The methane oxidation catalytic runs were performed in a fixed-bed reactor (i.d. 9 mm) operating at atmospheric pressure. The catalysts (1 g, 160-250 μm) diluted with quartz particles (300-500 μm) were pre-treated under a 5%O_2/Ar flow (100 cm^3 min^{-1}) at a temperature equal to their calcination temperature (773, 873, 973 or 1073 K) for 2 h. The reaction mixture was composed of 1%CH_4, 20%O_2 and N_2 as balance gas, with a

total flow of 500 cm^3 min^{-1} corresponding to a weight hourly space velocity (WHSV) of 300 cm^3 CH_4 h^{-1} g^{-1}. The reaction temperature was sequentially increased, with an interval of 25 K, from 473 to 773 K (heating). Thereafter, a cooling step, consisting of decreasing the reaction temperature from 773 to 473 K, was carried out without any pre-treatment in between. The evolution of the catalyst performance was studied by carrying out three heating/cooling consecutive cycles. Turnover frequency (TOF) values were estimated under differential reactor conditions (X_{CH4} < 13 %), at 623 K, as the moles of reacted methane per mole of surface palladium, as determined by H_2 chemisorption, and unit time. The apparent activation energy value was calculated assuming a first order reaction where a linear correlation existed between ln[-ln(1-X_{CH4})] and 1/T.

The stability of the catalysts was further investigated at 723 K for prolonged time on stream (52 h) and including a time span under humid conditions (17 h), where 10% water is added to the feed.

Additional experiments have been carried out at 723 K in order to assess the deactivation process when the catalytic reaction started under humid conditions (1%CH_4, 20%O_2, 10%H_2O and 69%He).

The analyses of the feed and effluent streams were performed using a MicroGC (Agilent 3000) equipped with a TCD detector.

3. Results and discussion

3.1. Textural properties

The N_2 physisorption isotherms corresponding to the bare support and the four Pd/HAP samples, respectively, are displayed in Fig. S1. It can be observed that all analyzed samples give similar shapes of both the isotherms and hysteresis loops. The adsorption branches are analogous to type II isotherms while the desorption process resembles a

H3 hysteresis loop. The latter is typically found over aggregates presenting slit-shaped pores [22]. Table 1 and Fig. S2 summarize the data extracted from the analysis of the isotherms. As expected, for the bare support, it can be observed that the increase in the calcination temperature systematically lowers the specific surface area, from 55 $m^2 g^{-1}$ (HAP-773), to 30 $m^2 g^{-1}$ (HAP-873), to 23 $m^2 g^{-1}$ (HAP-973) and to 13 $m^2 g^{-1}$, for HAP-1073 (Table 1). Furthermore, a comparison of the specific surface areas of the Pd-modified samples with those measured for the respective bare supports, treated at the same temperature, show significant differences (Fig. S2). The addition of Pd followed by calcination at 773 K does not induce significant changes in the textural properties of the support. By contrast, it seems that the impregnation of Pd and the successive treatment at higher temperatures (873-1073 K) result in a decreased S_{BET}, but to a lesser extent when compared to the trend showed by the bare support. Thus, the S_{BET} measured on Pd/HAP-1073 (18 $m^2 g^{-1}$) is significantly higher than that of HAP-1073 (13 $m^2 g^{-1}$). A similar behavior is observed for the Pd samples calcined at 873 K (41 $m^2 g^{-1}$) and 973 K (27 $m^2 g^{-1}$) with respect to their homologue bare supports (30 and 23 $m^2 g^{-1}$, respectively).

Interestingly, increasing the calcination temperature of the Pd catalyst markedly affects the pore size distribution, as shown in Fig. S3. The Pd/HAP-773 and Pd/HAP-873 samples exhibit a similar distribution consisting of a maximum centered at 33 nm and a shoulder around 51-52 nm, whereas the samples calcined at higher temperatures (Pd/HAP-973 and Pd/HAP-1073) display a notably broader peak centered at 54 and 51 nm, respectively. The changes observed in the textural properties of the investigated samples could be associated with a possible structural evolution induced by both the Pd addition and the calcination temperature.

3.2. Structural properties

The evolution of the structural properties of HAP and Pd/HAP samples with the calcination temperature were investigated by means of XRD techniques (Fig. 1a and Fig. 1b, respectively). The pattern of the HAP-773 bare support was characterized by the typical diffraction peaks ascribed to the hydroxyapatite structure (JCPDS 01-082-2956). Moreover, as can be observed in Fig. 1a, the diffractograms for the HAP samples heat-treated at 873, 973 and 1073 K, respectively, show a striking similarity with that of HAP-773. Nevertheless, the data reported in Table 1 reveal a significant improvement in the crystallinity degree (from 66.7%, for HAP-773, to 92%, for HAP-1073) and an increase in the crystallite size of HAP (from 46 Å for HAP-773, to 67.9 Å for HAP-1073) with T_c. In parallel, the calculations of the hydroxypatite lattice parameters reveal, though moderate, a systematic enlargement of its cell volume from 527.9 $Å^3$ for HAP-773, to 529 $Å^3$ for HAP-1073. This tendency could be assigned to a decomposition of impurities incorporated into the hydroxyapatite framework (such as structural carbonate species) [24].

Regarding the palladium-containing samples, their patterns evidence no lines belonging to palladium species; probably because of their high dispersion and/or their deposition as very small crystallites (Fig. 1b). However, as can be deduced from Table 1, irrespective of the calcination temperature, the addition of Pd decreases significantly the crystallite size of the HAP. Fig. S4 depicts the dependence of specific surface area on the HAP crystallite size values, as estimated using the XRD results. Expectedly, these data reveal a decrease in S_{BET} with increasing the crystallite size of HAP.

Figs. S5(a) and S5(b) compare the evolution of a-axis and hydroxyapatite cell volume, respectively, with T_c, for the HAP and Pd/HAP samples. The observed general trend suggests that there is a progressive expansion of the hydroxyapatite lattice for both the

HAP (from 527.9 to 529 $Å^3$) and Pd/HAP (from 527.8 to 530 $Å^3$) with increasing the calcination temperature. At 773 K, small differences can be observed between the HAP-773 bare support and the Pd/HAP-773 sample. At higher temperatures, with reference to the unpromoted samples, the addition of Pd seems to increase, even more, the lattice parameters of the hydroxyapatite. This effect is more pronounced on the samples calcined at 973 and 1073 K, respectively. For instance, the estimated hydroxyapatite cell volume increases from 529 $Å^3$, for HAP-1073, to 530 $Å^3$, for Pd/HAP-1073 (Fig. S5(b)). This trend contrasts those reported previously on HAP modified with Pt^{2+} [22], Mn^{2+}, Fe^{2+} and Co^{2+} [29]. On the latter, a shrinkage of the lattice parameters of HAP was observed due to an ion-exchange process involving cationic species exhibiting smaller ionic radius and more electronegative character compared to Ca^{2+} ions (Ca^{2+}: 1 Å and 1, respectively). Though Pd^{2+} has a smaller radius and a high electronegativity as well (0.86 Å and 2.2, respectively), its interaction with the HAP support does not lead to a contraction of its lattice. Taking into account the Ca-deficiency of our support (Ca/P = 1.60) we assume that the expansion of the hydroxyapatite lattice is most probably owing to an incorporation of Pd^{2+} ions into its surface cationic vacant sites. These results are in good agreement with those reported by Ma and Ellis [30] in their study on the Zn^{2+} occupation of Ca vacancy site in the HAP surface region. The diffusion of the Pd^{2+} ions into these vacancies seems to be easier at high calcination temperatures (≥ 873 K). Instead, the observed structural evolution sheds light, at least, on the occurrence of strong metal-support interactions (SMSI). To the best of our knowledge, no similar evidence was reported before, on the basis of a careful analysis of the structural properties of the HAP support.

3.3. UV-Visible-NIR spectroscopy

The evolution of the optical properties of the Pd species with the calcination temperature increase are examined by means of UV-visible-NIR DRS techniques. Fig. 2a displays the corresponding absorption spectra, recorded at room temperature. The spectrum of the bare support shows a set of absorption bands in the NIR region, centered at 1390, 1430 and 1920 nm, attributed to surface hydroxyl groups, structural OH^- and adsorbed water molecules, respectively [1]. Moreover, it contains a strong absorption peaked at 200 nm (UV domain) accompanied with a shoulder at 280 nm, due to $O^{2-} \rightarrow Ca^{2+}$ charge transfers [20,21,22].

The spectrum of the Pd/HAP-773 sample displays a broad band at 415 nm assigned to d–d ($\nu_1 + \nu_2$) transitions for Pd^{2+} ions in a tetrahedral coordination [1,20,31]. Moreover, when compared to the HAP bare support, the addition of Pd seems to intensify the UV bands which can be due to the contribution of $O^{2-} \rightarrow Pd^{2+}$ charge transfers. In the visible domain, the increase of T_c, from 773 to 873 K, leads to a much broader absorption, thereby indicating the coexistence of at least two different species containing Pd^{2+}. At higher T_c ($\geq$ 973 K), the charge transfer band shifts from 280 to 300 nm and new well-resolved features appear at 360 and 460 nm, which suggests a higher crystal field splitting energy. According to the literature data, the observed changes in the electronic properties of the Pd^{2+} ions would imply their structure evolution from tetrahedral (Td) to square planar geometry (D_{4h}) in oxygen rich environment [1,20,31]. In line with the progressive loss in the surface area, this behavior can be also correlated with an increase in the surface density of Pd species [20]. In parallel, we should underline a significant decrease in the intensity of the band assigned to the surface hydroxyl groups (1390 nm) with increasing calcination temperature, thus pointing out the occurrence of a surface dehydroxylation process. In correlation with our XRD data, it seems that on the Pd/HAP samples presenting SMSI

(calcined at $T_c \geq 873$ K) a fraction of Pd species exhibit a higher degree of oxidation and adopt D_{4h} coordination.

3.4. X-ray photoelectron spectroscopy

The influence of the calcination temperature on the composition and the distribution of the Pd species, laying on the surface of the calcined Pd/HAP catalysts, were investigated using XPS techniques. The spectra in the Pd $3d_{5/2}$ region, displayed in Fig. 3a, show a main peak around 336.6 ± 0.2 eV, assigned to PdO species [32]. Unexpectedly, another feature is detected at lower binding energies (335.3±0.2 eV) attributed to metallic Pd species [32,33]. As reported in Table 2, the Pd/HAP-773 sample contains the largest amounts of these metallic species (12.4%). This contribution is progressively less noticeable with the rise of T_c since it decreases significantly to 7.8% for Pd/HAP-873, 1.6% for Pd/HAP-973 and 2.3% for Pd/HAP-1073. This trend indicates that the formation of PdO is a slow process and/or that requires high calcination temperatures to be stabilized. Instead, we might think that the PdO phase could suffer from drastic changes during its cooling step, induced by their reactivity with surface species. In this sense, Tessier et al. [31] reported that the abundance of surface hydroxyls on alumina might reduce Pd^{2+} ions, as described by the following reaction:

$$Pd^{2+} + 2\ OH^- \rightarrow Pd^o + \tfrac{1}{2}\ O_2 + H_2O \qquad (3)$$

In accordance with this proposal, the very low contribution of the Pd metallic species on the samples calcined at high temperatures (973 and 1073 K) can be associated with the low density of surface hydroxyl groups. This is in line with the UV-vis-NIR results which evidence that a high-temperature treatment favors the dehydroxylation of the HAP surface. There is still another possibility consisting on the encapsulation of the

oxidized species of Pd, at high temperatures, which avoid their reduction process during the cooling step. This interpretation is very consistent with the TEM observations to be commented below.

The O 1s spectra of the catalysts are displayed in Fig. 3b. All samples show a main peak centered at 531 ± 0.2 eV, attributed to lattice oxygen species [34,35]. The deconvolution of the spectra evidences, moreover, the presence of two additional O 1s peaks, centered at 532.4 ± 0.3 eV and 533.5 ± 0.3 eV, corresponding to surface -O-C and C-O-C species, respectively [35]. The presence of these carbonaceous species is unavoidable because during the thermal treatment and the following cooling step the hydroxyapatite is susceptible to contamination coming from atmospheric CO_2 [24]. Interestingly, the contribution of these species seems to increase with T_c, in consistency with an increase observed in the surface C/P molar ratio (Table 2). Moreover, it is not excluded that these features overlap that assigned to OH species which usually appear at BE > 531 eV [34].

On the other hand, for all Pd catalysts the surface Ca/P ratio (1.42-1.46) is slightly lower than that estimated for the HAP bare support (1.5). In parallel, the surface Pd/P ratio remains almost constant (0.007-0.008) and agree well with the values given by the ICP analysis, thus suggesting that the Pd species are uniformly exposed on the catalysts near surface.

3.5. Reducibility of the catalysts

The reducibility of the Pd species was investigated by H_2-TPR techniques. Fig. S6 and Fig. 4 include the reduction profiles for the HAP-773 bare support and all Pd-modified samples, respectively.

The Pd/HAP-773 catalyst presents a typical diagram corresponding to the reduction of the supported PdO species. The first peak centered at 300 K is attributed to the reduction of PdO (α species) while the second one (331 K) corresponds to a release of H_2 ascribed to the decomposition of palladium hydride (Pd-H) [18]. Generally, the latter is formed at low temperature involving the surface metallic Pd. At higher reduction temperatures (577 K) an additional less intense peak can be observed, being probably owing to the HAP support (Fig. S6). A similar H_2-TPR trace can be noticed for the Pd/HAP-873 sample. However, when T_c is increased from 873 to 973 K the peak assigned to PdO species becomes relatively much broader and shifts towards somewhat higher temperature (from 301 to 310 K). Interestingly, the profile of the Pd/HAP-1073 sample does not show the negative peak observed on the rest of the catalysts. Its reduction process gives rise to two positive features peaked at 308 K (α species) and 329 K (β species), respectively, revealing the existence of two distinct reducible Pd species. Note that the negative peak is probably masked by the occurrence of the second feature (β species). The contribution of the α and β species accounts for 55.9% and 44.1%, respectively, of the total reducible Pd species (Table 3). We assume that the second form that can only be unequivocally identified on the sample calcined at 1073 K corresponds most likely to PdO species strongly interacting with the HAP. It is worth noting that the presence of the low temperature doublet was also observed in a variety of Pd supported catalysts [36-38]. For instance, Ivanova et al. [36] found a main peak at 296 K and a shoulder, at 315 K, when they treated their Pd/Al_2O_3 catalyst at 1073 K. They attributed the occurrence of the latter to the reduction of PdO particles interacting more strongly with the support. In the case of a zeolite support [38], presenting a high capacity for ionic exchange, it was reported that the reduction doublet could be ascribed

to Pd^{2+} ions located in different sites of the support framework (namely supercage and sodalite cage sites, respectively).

On the other hand, according to Table 3, the H_2/Pd molar ratios are very close to the theoretical value for the reduction of a stoichiometric PdO, in the case of Pd/HAP-973 and Pd/HAP-1073 catalysts (0.95 and 0.97, respectively). By contrast, Pd/HAP-773 and Pd/HAP-873 samples exhibit lower values (0.73 and 0.75, respectively). In good agreement with the XPS studies, these results point out that, on these two samples, there is a significant contribution of Pd species presenting a lower oxidation state.

In addition, the reducibility of the Pd/HAP catalysts was also investigated by CH_4-TPR techniques. The diagrams corresponding to desorption of CO_2 are displayed in Fig. 5. Over the Pd/HAP-773 sample, the CO_2 production starts at 470 K followed by a set of three peaks located at 540, 600 and 710 K. Interestingly, as can be observed in Fig. S7(a), the peak at 600 K is accompanied by desorption of CO, while that centered at 710 K occurs with significant production of both CO and H_2. (Fig. S7(a) and Fig. S7(b), respectively). On the basis of these observations and data from the literature, we assume that the occurrence of the first peak can only be unequivocally attributed to the reduction of PdO by methane, according to the following reaction [2,39]:

$$4\ PdO + CH_4 \rightarrow 4\ Pd + CO_2 + 2\ H_2O \qquad (4)$$

As the calcination temperature is increased, the onset temperature of the PdO reduction progressively shifts towards higher values. Moreover, though the position of the peak at 540 K remains almost unchanged, its intensity seems to systematically increase with T_c. As shown in Table 3, this would mainly consist of an increase in the reducible fraction of Pd species, from 20.6% for Pd/HAP-773 to 27.9% for Pd/HAP-873, to 41.6% for Pd/HAP-973 and 54.1% for Pd/HAP-1073. This trend agrees with that given by H_2-TPR data. Besides, the different reducibility of the Pd samples, which is due to very subtle

structural and oxidation state changes, would mainly account for their capacity to activate the methane molecules upon increasing T_c.

On the other hand, the high production of CO, CO_2 and H_2 observed above 540 K, could be associated with the occurrence of side reactions involving methane steam reforming (5), reverse water-gas shift (6), CO disproportionation (7) and methane cracking (8), among others [2,23,39]:

$$CH_4 + H_2O \leftrightarrow CO + 3\ H_2 \quad (5)$$

$$CO_2 + H_2 \leftrightarrow CO + H_2O \quad (6)$$

$$2\ CO \rightarrow C + CO_2 \quad (7)$$

$$CH_4 \rightarrow C + 2\ H_2 \quad (8)$$

3.6. Transmission electron microscopy (TEM)

Fig. 6 includes the TEM images taken for all Pd catalysts, reduced at 473 K. In all cases, quasi spherical particles of Pd are observed. The Pd/HAP-773 sample shows a narrow distribution of the particle sizes, ranged between 4 and 12 nm, and the estimated average diameter is found to be around 7 nm (Table 4). Upon increasing the calcination temperature up to 973 K, the distribution becomes broader and a progressive increase in the Pd particle size can be observed (8 nm, for Pd/HAP-873 and 9.7 nm, for Pd/HAP-973). Interestingly, when T_c is increased from 973 to 1073 K, the average size of Pd particles remains almost constant (9.7-9.9 nm). This invariability is visible despite the fact that a significant loss in the surface area is observed (from 27 $m^2\ g^{-1}$ at 973 K, to 18 $m^2\ g^{-1}$ at 1073 K), thereby evidencing a possible stabilization of the Pd particles. In fact, in contrast to the rest of the catalysts, a high-magnification image for the Pd/HAP-1073 sample reveals the presence of a HAP thin layer covering Pd large particles (Fig. 7). These observations point out this encapsulation originated from the migration of the

support onto them. A similar behavior was also found by Tang et al. [26] in their study on HAP supported platinum-group metal catalysts. They attributed this effect, favored only at high temperatures, to the occurrence of strong metal-support interactions (SMSI). This is also in good agreement with our H_2-TPR data for the Pd/HAP-1073 catalyst which have revealed the presence of Pd reducible species presenting strong interactions with the HAP support. In order to help visualize the meaning of our conclusions we summarize in Fig. 7b the distribution of the Pd species present in the Pd/HAP-1073 sample.

A comparison of the Pd dispersion (TEM) with that estimated by H_2 chemisorption reveals a slight difference in the case of the Pd/HAP-773 and Pd/HAP-873 samples. By contrast, on the Pd/HAP-973 and Pd/HAP-1073 catalysts the Pd dispersion values measured by H_2 chemisorption are significantly lower (7.5% and 4.5%, respectively). This suggests that a large fraction of the surface Pd species is not accessible to the gas phase (representing 22.7%, on Pd/HAP-973, and 54.5%, on Pd/HAP-1073). In turn, these results can be explained by the encapsulation of Pd particles, as observed by TEM.

On the other hand, given the textural differences found among the investigated samples it is worth analyzing the relationship between the surface density of Pd species and their estimated dispersion. Table 4 reports the values of the interparticle distance for all Pd catalysts estimated according to a procedure reported elsewhere [28,40-42]. It can be observed that among all investigated samples the Pd/HAP-973 gives the largest interparticle distance (189 nm), followed by Pd/HAP-873 (174 nm), Pd/HAP-773 (162 nm) and Pd/HAP-1073 (159 nm).

3.7. CO adsorption studies

Figs. 8a and 8b display the FTIR spectra of CO adsorption and desorption, respectively, for the Pd/HAP samples reduced at 473 K. The CO adsorption spectrum recorded on Pd/HAP-773 sample (Fig. 8a) shows a typical band attributed to CO linearly bonded on Pd^{o} sites (2090 cm^{-1}) and a much broader feature assigned to bridge-bonded CO (1935-1995 cm^{-1}) [31]. Interestingly, the rise of T_c, from 773 to 1073 K induces a progressive decrease in the intensity of these bands. Moreover, after evacuation for 45 min (Fig. 8b), the CO linearly bonded band disappears completely for the samples calcined at high temperatures (973 and 1073 K, respectively). By contrast, this is still detected on the Pd/HAP-773 and Pd/HAP-873 samples, although it becomes considerably less intense and shifts towards lower wavenumbers (from 2090 to 2077 cm^{-1}). Simultaneously, in the characteristic region of the bridge-bonded CO species a well resolved band, centered at 1975 cm^{-1}, accompanied by two shoulders, located at 1935 and 1867 cm^{-1}, can be discerned. According to previous reports, the suppression of CO chemisorption over the samples calcined at high temperatures confirms once again the occurrence of SMSI [26].

Fig. S8 reports the evolution of the FTIR CO adsorption spectra, recorded at 5 min interval during 45 min. Special attention is paid to the analysis of the characteristic regions of adsorbed water molecules (2700-3720 cm^{-1}) and carbonates species (1280-1740 cm^{-1}), respectively [1]. On the Pd/HAP-773 sample, with CO adsorption time, there is a progressive increase in the intensity of the bands assigned to adsorbed carbonates and adsorbed water. Simultaneously, a band ascribed to hydroxyl groups (3570 cm^{-1} [1]) decreases with time of CO adsorption, which becomes negative after 30 min treatment. This behavior would imply a slow dehydroxylation process, through CO adsorption, involving reactive OH species on the HAP surface. Thus, large amounts of produced water and carbonates are adsorbed on the surface. This effect occurs to a

lesser extent upon increasing T_c, as a progressive decrease in the intensity of the band assigned to water and carbonates species was observed. In turn, this is indicative of the decrease in the density of hydroxyl groups, in good agreement with UV-vis-NIR and XPS data.

3.8. Ultimate oxygen storage capacity (OSC)

The ultimate OSC studies for the Pd/HAP catalysts in the temperature range between 623 and 773 K are summarized in Fig. 9. By means of these experiments valuable information about the maximum ability of the catalysts to be re-oxidized can be gained. It should be noted that the catalysts were pre-reduced at 773 K under 5%H_2/Ar for 1 h. It can be observed that, for all Pd/HAP samples, the OSC activity increases with temperature. Moreover, the OSC values given by the Pd/HAP-773 sample are the highest ones in the whole range of the investigated temperatures. At 773 K, the oxygen uptake (23.1 $\mu mol_{O2}\ g^{-1}$) is very close to the theoretical value required for the formation of stoichiometric PdO (23.5 $\mu mol_{O2}\ g^{-1}$). This result points out that the deposition of metallic Pd, deduced from XPS and H_2-TPR data, occurs most likely during the sample cooling step; thereby the reaction of PdO with surface hydroxyls.

As the calcination temperature is increased, the OSC values are progressively lower. For instance, in contrast to Pd/HAP-773, on Pd/HAP-1073 a large fraction of Pd remains in the reduced state after being exposed to oxygen pulses (up to 773 K). Its OSC does not exceed 12.2 $\mu mol_{O2}\ g^{-1}$ at 773 K, which means that only 51.9% of the Pd metal is oxidized into PdO. Thus, there is still a second fraction, representing the 48.1% of the supported Pd, which does not oxidize probably because it is not accessible to the gas phase; which agrees with the significant growth of the Pd particles. These results are consistent with a previous study reported by Roth et al. [43] demonstrating that the

small Pd particles exhibited a higher tendency to be oxidized compared with larger ones. In sum, as for the redox properties of the Pd/HAP samples, we can conclude that adopting a high-temperature treatment seems to promote PdO reduction, but it hinders Pd^o reoxidation, as shown by CH_4-TPR and OSC data, respectively.

3.9. Catalytic activity

The influence of the calcination temperature on the catalytic activity of the Pd/HAP samples in the methane oxidation reaction was investigated in the temperature range of 473-773 K. Note that Pd/HAP-773, Pd/HAP-873, Pd/HAP-973 and Pd/HAP-1073 catalysts were pre-treated at 773, 873, 973 and 1073 K, respectively, under a 5%O_2/He flow for 2 h. The reproducibility of the performances was examined by carrying out three heating/cooling consecutive cycles. Fig. 10 includes the light-off curves representing the conversion recorded from the first heating cycle. Over the Pd/HAP-773 catalyst, the methane conversion starts around 525 K and increases slowly with the reaction temperature to reach 23% at 650 K, 61% at 700 K and finally approaches 100% at 773 K. However, a significant decrease in the activity is evident over the samples heat-treated at higher temperatures. Among all prepared catalysts, the Pd/HAP-973 exhibits the poorest performance, since its activity does not exceed 20% at 700 K. Thus, the initial activity follows this general trend: Pd/HAP-773 > Pd/HAP-873 > Pd/HAP-1073 > Pd/HAP-973. The superiority of the Pd/HAP-773 sample in terms of the overall initial activity can be associated with both the improved textural properties and the high Pd dispersion compared with the rest of the catalysts. Moreover, this catalyst has a high OSC and contains the largest amounts of both acid and basic sites (Table 4), which probably play a role in facilitating the methane oxidation reaction [44].

Fig. 11 and Fig. 12 include the evolution of methane conversion and the temperature for 50% conversion (T_{50}) values, respectively, during the three heating/cooling cycles over all investigated catalysts. With reference to the first heating ramp, over the Pd/HAP-773 catalyst the activity significantly decreases during the subsequent cooling step, since T_{50} increases from 685 to 694 K (Fig. 12). The extent of its deactivation, however, seems to be much lower during the following reaction cycles, up to the second cooling ramp. Thereafter, it seems to maintain a stable performance. By contrast, as for Pd/HAP-873 and Pd/HAP-973 samples the first cooling branch shows a clear enhancement of their activity when compared with their first heating ramp (Fig. 11 and Fig. 12). Then, they undergo a smooth activation process during the following reaction cycles. Interestingly, on the Pd/HAP-1073 catalyst a slight activation could be observed with the successive heating/cooling cycles, thus suggesting its high stability (Fg. 11 and Fig. 12). On the other hand, the observed difference in the activation/deactivation process between the Pd/HAP-773 sample and the rest of the catalysts could be related to drastic changes occurring on their surface via different pathways including a possible re-dispersion of the Pd active species. In fact, data reported in Table 4 reveal a significant loss in the Pd dispersion, after submitting the Pd/HAP-773 catalyst to three heating/cooling cycles of the reaction (from 21.4% to 16.3%). Conversely, the catalysts calcined at higher temperatures (873-1073 K) show an increase in the Pd dispersion.

Table 5 summarizes the catalytic data extracted from the analysis of the third heating light-off curve, considering that in this period the catalysts show a certain stability. Therefore, the TOF values are estimated using the Pd dispersion data, as determined for the spent catalysts. It should be highlighted that our values (0.049-0.074 s^{-1}) somewhat outperform those reported by Velin et al. [11] in their study on the activity of Pd/Al_2O_3 catalysts (0.051-0.057 s^{-1}). Moreover, upon increasing T_c, a systematic increase in TOF

can be noted; being the Pd/HAP-1073 catalyst the most active one (0.074 s^{-1}), followed by Pd/HAP-973 (0.071 s^{-1}), Pd/HAP-873 (0.053 s^{-1}) and Pd/HAP-773 (0.049 s^{-1}), respectively. This tendency matches well with the ability of the catalysts to activate CH_4 molecules, as reported by CH_4-TPR. In this sense, it is accepted that in methane oxidation reaction the splitting of the methane molecule is the rate-limiting step [50]. It should be highlighted that the Pd/HAP-1073 shows the most efficient Pd species despite it contains the relatively largest Pd particles. This points out that, over our Pd/HAP system, methane oxidation reaction is a structure-sensitive reaction, in agreement with previous studies [46,47]. Our characterization results evidence that the occurrence of SMSI, between Pd and HAP, is rather favored at high calcination temperatures. This increase in the Pd-HAP interaction strength seems to (i) expand the HAP lattice, (ii) change the Pd^{2+} coordination from Td to D_{4h} geometry, (iii) promote PdO reduction and (iv) suppress CO chemisorption. In turn, these proven characteristics do benefit the efficiency and stability of the Pd species in methane oxidation reaction. Nevertheless, the lower efficiency of the Pd particles exposed on the Pd/HAP-773 and Pd/HAP-873 samples seems to be compensated by their improved textural properties and Pd dispersion; which probably increase their overall activity. In fact, a comparison based on the specific activity per gram of sample (r) shows that, at 623 K, the most active catalyst is Pd/HAP-873 (0.48 $\mu mol_{CH4}\ g^{-1}\ s^{-1}$) whereas the sample treated at a higher temperature (Pd/HAP-1073) exhibits the lowest activity (0.24 $\mu mol_{CH4}\ g^{-1}\ s^{-1}$).

It is worth noting that the apparent activation energy (E_a) estimated for our Pd/HAP catalysts (67-84 kJ mol^{-1}) are similar to those found for a number of Pd catalysts reported previously [48,49]. Escandón et al. [48] found E_a values ranging between 73-80 kJ mol^{-1} over Pd/Al_2O_3, Pd/SiO_2, Pd/TiO_2 and Pd/ZrO_2 catalysts, irrespective of the

initial oxidation state of Pd. E_a values close to those estimated by us were also reported by Petrov et al. [49] over palladium based zeolite catalysts (75-84 kJ mol^{-1}).

The capacity of the Pd/HAP catalysts to endure more severe conditions has been investigated at 723 K for a more prolonged time on stream (52 h) including a period under humid conditions as well, where 10% water is added to the feed. The data reported in Fig. 13 reveal that the Pd/HAP-773 sample exhibits the highest initial conversion (97%), followed by Pd/HAP-1073 (89%), Pd/HAP-873 (88%) and Pd/HAP-973 (80%). Considering the high conversion values achieved, this order could be connected with differences affecting the diffusion of the reactant/products of the reaction. Particularly, the interparticle distance (X_i) was found to be an important structural parameter of nanoscale catalysts, which can significantly affect mass transport during chemical reactions [28,40-42]. Interestingly, a linear relationship is derived between the initial activity and X_i for the samples calcined at temperatures ranging between 773 and 973 K (Fig. 14). Therefore, the activity is favored over the catalyst presenting a shorter interparticle distance. It is worth noting that the peculiar behavior shown by the sample calcined at the highest temperature (1073 K) can be associated with the encapsulation of a large fraction of Pd active phase. In order to evaluate the difference in the internal diffusion resistance between the Pd/HAP-773 and Pd/HAP-973 catalysts additional experiments have been carried out under different contact time values (W/F_{CH4} ranging between 9.3 and 74.6 g h mol^{-1}). As can be deduced from Fig. S10(a), the activity of the Pd/HAP-973 catalyst starts to be strongly influenced by the internal diffusion at W/F_{CH4} = 28 g h mol^{-1}. By contrast, the impact of the internal diffusion seems to be much lower in the case of the Pd/HAP-773 catalyst (Fig. S10(b)).

On the other hand, over the Pd/HAP-773 catalyst, the activity decreases slowly to reach its minimum value (83%) after 18 h TOS, which corresponds to the highest activity loss

(16.9%) compared with the samples calcined at higher temperatures (9.6-10.8%) (Table 5). As stated before, the largest deactivation loss that suffers the Pd/HAP-773 catalyst is consistent with its lower resistance to sintering (Table 4). On the Pd/HAP-873 sample, however, the deactivation process seems to be somewhat faster and undergoes 10.8% activity loss after only 12 h time on stream. By contrast, on the Pd/HAP-973 and Pd/HAP-1073 catalysts the activity rapidly decreases after 2 h reaction (by 10.8% and 9.6%, respectively) and seems to maintain values close to 71% and 81%, respectively, up to 25 h TOS. We should underline that, despite its poor textural properties, the Pd/HAP-1073 sample (18 m^2 g^{-1}) exhibits CH_4 conversion values, after 25 h TOS, close to those found over the Pd/HAP-773 (54 m^2 g^{-1}) and Pd/HAP-973 (41 m^2 g^{-1}) catalysts. This is a remarkable finding indicating that the activity would mainly depend on the type of the metal-support interactions, being significantly stronger on the Pd/HAP-1073 sample, as mentioned above.

The differences noticed in the deactivation rate, under dry conditions, suggest that the catalysts suffer from distinct surface re-structuring processes. Previous studies correlated the Pd catalyst deactivation with surface hydroxyl groups accumulation on its active sites [2,4,5,45,54], according to the following Eq [45]:

$$H_2O + 2\ S^* + \tfrac{1}{2}\ O_2 \rightarrow 2\ S^*\text{-}OH \qquad (9)$$

Though their occurrence is unavoidable, the accumulation rate of these poisoning species was found to be slower on catalysts presenting high specific surface area [54]. This is in line with the slow deactivation rates that undergo our catalysts exhibiting higher S_{BET} (Pd/HAP-773 and Pd/HAP-873). These catalysts are also characterized by a high ability to re-oxidize metallic Pd into PdO, as shown by the OSC data. We conclude that owing to these properties the deactivation of the Pd/HAP-773 and Pd/HAP-873 catalysts occurs through a relatively slower process [54].

The effect of H_2O addition has also been examined by monitoring the CH_4 conversion at the same temperature (723 K) for 17 h. As shown in Fig. 13, over all tested catalysts the addition of water lowers significantly the methane conversion, by around 49.4-51.8% (Table 5). For instance, over the Pd/HAP-773 catalyst the conversion decreases from 83% to 40 % whereas on Pd/HAP-973 it decreases from 71% to 29%. Nevertheless, the extent of deactivation is not as profound as that reported by Persson et al. [50] for a Pd/Al_2O_3 catalyst. In that case, the addition of water decreases the methane conversion from 97% to 12%. A similar behavior was reported by Mihai et al. [2] in their study on a Pd/Al_2O_3 catalyst. They attributed the observed deactivation to the presence of water which inhibits the re-oxidation of palladium. By using operando FTIR spectroscopy analyses, Velin et al. [11] observed that humid conditions caused severe hydroxylation of their Pd/Al_2O_3 system that was detrimental for the methane oxidation TOF. However, various works described the deactivation of Pd catalysts by water as a reversible process owing to the existence of the equilibrium $PdO + H_2O \leftrightarrow Pd(OH)_2$, where $Pd(OH)_2$ is an inactive phase for methane oxidation [51-53]. We think that the latter explanation is quite prevalent to describe the deactivation process of our catalysts under humid conditions. A proof of that, as shown in Fig. 13, when water flow is stopped, all investigated samples tend to rapidly recover their activity shown before the addition of water, thus indicating the reversibility of their deactivation process. It is worth noting that the analysis of all spent catalysts evidenced that no significant changes are noted in their BET surface area, thus pointing out that a possible degradation of the HAP support is discarded.

In order to provide insight into the deactivation process of the catalysts in the presence of water, additional experiments have been carried out at 723 K for a prolonged TOS (36 h). As expected, under humid conditions all catalysts exhibit lower initial activity

(Fig. 15) compared with that observed under dry conditions (Fig. 13). Moreover, addition of water results in a significant change in the initial activity order which becomes: Pd/HAP-773 (70%) > Pd/HAP-873 (54%) > Pd/HAP-973 (46%) > Pd/HAP-1073 (27%). It should be outlined that the extent of deactivation of the catalysts calcined at T ≤ 973 K (21-31%) is more profound than that observed under dry conditions (10.8-16.9%). By contrast, the activity of the Pd/HAP-1073 sample seems to proceed via a different pathway (Fig. 15). On the latter, it can be observed a gradual increase in the catalytic activity from 27% to 37%, during the first 24 h TOS. This behavior would mainly be related to an increase in the number of the exposed Pd active sites. It should be noted that on the fresh Pd/HAP-1073 sample, besides the presence of easily reducible Pd species, a fraction of Pd particles were found encapsulated by a thin support layer. Probably, this distribution changes progressively when the catalyst is submitted to the reaction mixture. In fact, TEM observations on the spent Pd/HAP-1073 catalyst evidence the absence of encapsulated particles of Pd (not displayed). Moreover, with reference to the fresh sample, the H_2-TPR diagram of the spent Pd/HAP-1073 sample (Fig. S11) reveals the disappearance of the high temperature peak (329 K, β species) and the increase in the intensity of the peak due to the surface PdO species (310 K, α species). These results suggest that the progressive activation of this sample with TOS was induced by the de-encapsulation of the Pd active phase under the reaction mixture.

4. Conclusions

The present study offers a detailed picture of the chemical, structural and catalytic properties of a series of Pd/HAP samples with a Pd loading close to 0.5 wt.%. Special attention has been paid to the study of the influence of the calcination temperature on

the above-mentioned properties. Upon increasing the calcination temperature, from 773 to 1073 K, the properties of the supported PdO phases are significantly modified, as a result of an evolution in the strength of their interactions with the HAP support. Our characterization results evidence that the occurrence of SMSI, between Pd and HAP, is rather favored at high calcination temperatures. This increase in the Pd-HAP interaction strength seems to (i) expand the HAP lattice, (ii) change the Pd^{2+} coordination from Td to D_{4h} geometry, (iii) promote PdO reduction and (iv) suppress CO chemisorption. These entire properties do compensate the poor textural properties and benefit the efficiency and stability of the Pd species in methane oxidation reaction.

Acknowledgments

The financial support for this work provided by Ministerio de Economía y Competitividad (CTQ2015-73219-JIN (AEI/FEDER/UE) and CTQ2016-80253-R (AEI/FEDER/UE)), Basque Government (GIC IT-1297-19) and the University of the Basque Country UPV/EHU (PIF15/335) is gratefully acknowledged. Likewise, the technical support provided by SGIker (UPV/EHU) is gratefully acknowledged.

References

[1] Z. Boukha, M. Kacimi, M. Ziyad, A. Ensuque, F. Bozon-Verduraz, Comparative study of catalytic activity of Pd loaded hydroxyapatite and fluoroapatite in butan-2-ol conversion and methane oxidation, J. Mol. Catal. A-Chem. 270 (2007) 205-213.

[2] O. Mihai, G. Semdler, U. Nylén, M. Olofsson, L. Olsson, The effect of water on methane oxidation over Pd/Al_2O_3 under lean, stoichiometric and rich conditions, Catal. Sci. Technol. 7 (2017) 3084-3096.

[3] R. Gholami, M. Alyani, K.J. Smith, Deactivation of Pd catalysts by water during low temperature methane oxidation relevant to natural gas vehicle converters, Catalysts 5 (2015) 561-594.

[4] I. Friberg, N. Sadokhina, L. Olsson, The effect of Si/Al ratio of zeolite supported Pd for complete CH_4 oxidation in the presence of water vapor and SO_2, Appl. Catal. B-Environ. 250 (2019) 117-131.

[5] I. Friberg, N. Sadokhina, L. Olsson, Complete methane oxidation over Ba modified Pd/Al_2O_3: The effect of water vapour, Appl. Catal. B-Environ. 231 (2018) 242-250.

[6] G. Ercolino, P. Stelmachowski, G. Grzybek, A. Kotarba, S. Specchia, Optimization of Pd catalysts supported on Co_3O_4 for low-temperature lean combustion of residual methane, Appl. Catal. B-Environ. 206 (2017) 712-725.

[7] M. Hoffmann, S. Kreft, G. Georgi, G. Fulda, M. Pohl, D. Seeburg, C. Berger-Karin, E.V. Kondratenko, S. Wohlrab, Improved catalytic methane combustion of Pd/CeO_2 catalysts via porous glass integration, Appl. Catal. B-Environ. 179 (2015) 313-320.

[8] R. Gholami, K.J. Smith, Activity of PdO/SiO_2 catalysts for CH_4 oxidation following thermal treatments, Appl. Catal. B-Environ. 168-169 (2015) 156-163.

[9] J. Park, J.H. Cho, Y.J. Kim, E.S. Kim, H.S. Han, C. Shin, Hydrothermal stability of Pd/ZrO_2 catalysts for high temperature methane combustion, Appl. Catal. B-Environ. 160-161 (2014) 135-143.

[10] A. Baylet, P. Marécot, D. Duprez, P. Castellazzi, G. Groppi, P. Forzatti, In situ Raman and in situ XRD analysis of PdO reduction and Pd° oxidation supported on γ-Al_2O_3 catalyst under different atmospheres, Phys. Chem. Chem. Phys. 13 (2011) 4607-4613.

[11] P. Velin, M. Ek, M. Skoglundh, A. Schaefer, A. Raj, D. Thompsett, G. Smedler, P. Carlsson, Water inhibition in methane oxidation over alumina supported palladium catalysts, J. Phys. Chem. C. 123 (2019) 25724-25737.

[12] S. A. Yashnik, Z.S. Vinokurov, A.V. Salnikov, A.V. Ishchenko, V.V. Kaichev, Z.R. Ismagilov, Temperature hysteresis in the reaction of methane oxidation on a palladium-doped manganese hexaaluminate catalyst, Kinet. Catal. 59 (2018) 70-82.

[13] J.K. Edwards, J. Pritchard, M. Piccinini, G. Shaw, Q. He, A.F. Carley, C.J. Kiely, G.J. Hutchings, The effect of heat treatment on the performance and structure of carbon-supported Au-Pd catalysts for the direct synthesis of hydrogen peroxide, J. Catal. 292 (2012) 227-238.

[14] P. Castellazzi, G. Groppi, P. Forzatti, A. Baylet, P. Marécot, D. Duprez, Role of Pd loading and dispersion on redox behaviour and CH_4 combustion activity of Al_2O_3 supported catalysts, Catal. Today 155 (2010) 18-26.

[15] Z. Boukha, J.L. Ayastuy, M. Cortés-Reyes, L.J. Alemany, J.R. González-Velasco, M.A. Gutiérrez-Ortiz, Catalytic performance of Cu/hydroxyapatite catalysts in CO preferential oxidation in H_2-rich stream, Int. J. Hydrogen Energ. 44 (2019) 12649-12660.

[16] Z. Boukha, J.L. Ayastuy, M. Cortés-Reyes, L.J. Alemany, M.A. Gutiérrez-Ortiz, J.R. González-Velasco, Catalytic properties of cobalt-promoted Pd/HAP catalyst for CO-cleanup of H_2-rich stream, Int. J. Hydrogen Energ. 43 (2018) 16949-16958.

[17] Z. Boukha, J.L. Ayastuy, J.R. González-Velasco, M.A. Gutiérrez-Ortiz, Water-gas shift reaction over a novel Cu-ZnO/HAP formulation: Enhanced catalytic performance in mobile fuel cell applications, Appl. Catal. A-Gen. 566 (2018) 1-14.

[18] Z. Boukha, J.L. Ayastuy, J.R. González-Velasco, M.A. Gutiérrez-Ortiz, CO elimination processes over promoter-free hydroxyapatite supported palladium catalysts, Appl. Catal. B-Environ. 201 (2017) 189-201.

[19] Z. Boukha, M. Gil-Calvo, B. de Rivas, J.R. González-Velasco, J.I. Gutiérrez-Ortiz, R. López-Fonseca, Behaviour of Rh supported on hydroxyapatite catalysts in partial oxidation and steam reforming of methane: On the role of the speciation of the Rh particles, Appl. Catal. A-Gen. 556 (2018) 191-203.

[20] Z. Boukha, J. González-Prior, B. de Rivas, J.R. González-Velasco, R. López-Fonseca, J.I. Gutiérrez-Ortiz, Pd supported catalyst for gas-phase 1,2-dichloroethane abatement: Efficiency and high selectivity towards oxygenated products, J. Ind. Eng. Chem. 57 (2018) 77-88.

[21] Z. Boukha, J. González-Prior, B. Rivas, J.R. González-Velasco, R. López-Fonseca, J.I. Gutiérrez-Ortiz, Synthesis, characterisation and behaviour of Co/hydroxyapatite catalysts in the oxidation of 1,2-dichloroethane, Appl. Catal. B-Environ. 190 (2016) 125-136.

[22] Z. Boukha, J.R. González-Velasco, M.A. Gutiérrez-Ortiz, Platinum supported on lanthana-modified hydroxyapatite samples for realistic WGS conditions: On the nature of the active species, kinetic aspects and the resistance to shut-down/start-up cycles, Appl. Catal. B-Environ. 270 (2020).

[23] Z. Boukha, M. Kacimi, M.F.R. Pereira, J.L. Faria, J.L. Figueiredo, M. Ziyad, Methane dry reforming on Ni loaded hydroxyapatite and fluoroapatite, Appl. Catal. A-Gen. 317 (2007) 299-309.

[24] Z. Boukha, M.P. Yeste, M.Á. Cauqui, J.R. González-Velasco, Influence of Ca/P ratio on the catalytic performance of Ni/hydroxyapatite samples in dry reforming of methane, Appl. Catal. A-Gen. 580 (2019) 34-45.

[25] U. Iriarte-Velasco, J.L. Ayastuy, Z. Boukha, R. Bravo, M.Á. Gutierrez-Ortiz, Transition metals supported on bone-derived hydroxyapatite as potential catalysts for the Water-Gas Shift reaction, Renew. Energ. 115 (2018) 641-648.

[26] H. Tang, Y. Su, Y. Guo, L. Zhang, T. Li, K. Zang, F. Liu, L. Li, J. Luo, B. Qiao, J. Wang, Oxidative strong metal-support interactions (OMSI) of supported platinum-group metal catalysts, Chem. Sci. 9 (2018) 6679-6684.

[27] E. Landi, A. Tampieri, G. Celotti, S. Spiro, Densification behaviour and mechanisms of synthetic hydroxyapatites, J. Eur. Ceram. Soc. 20 (2000) 2377-2387.

[28] M. Watanabe, H. Sei, P. Stonehart, The influence of platinum crystallite size on the electroreduction of oxygen, J. Electroanal. Chem. 261 (1989) 375-387.

[29] M.E. Zilm, L. Chen, V. Sharma, A. McDannald, M. Jain, R. Ramprasad, M. Wei, Hydroxyapatite substituted by transition metals: Experiment and theory, Phys. Chem. Chem. Phys. 18 (2016) 16457-16465.

[30] X. Ma, D.E. Ellis, Initial stages of hydration and Zn substitution/occupation on hydroxyapatite (0001) surfaces, Biomaterials 29 (2008) 257-265.

[31] D. Tessier, A. Rakai, F. Bozon-Verduraz, Spectroscopic study of the interaction of carbon monoxide with cationic and metallic palladium in palladium-alumina catalysts, J. Chem. Soc. Faraday Trans. 88(5) (1992) 741-749.

[32] F. Huang, J. Chen, W. Hu, G. Li, Y. Wu, S. Yuan, L. Zhong, Y. Chen, Pd or PdO: Catalytic active site of methane oxidation operated close to stoichiometric air-to-fuel for natural gas vehicles, Appl. Catal. B-Environ. 219 (2017) 73-81.

[33] S. Iqbal, M.L. Shozi, D.J. Morgan, X-ray induced reduction of rhenium salts and supported oxide catalysts, Surf. Interface Anal. 49 (2017) 223-226.

[34] T. Onoki, A. Nakahira, Effects of titanium polishing environments, on bonding behavior of hydroxyapatite ceramics and titanium, by hydrothermal hot-pressing, Mater. Sci. Eng. B. 173 (2010) 72-75.

[35] S. Ye, Z. Li, T. Song, D. Cheng, Q. Xu, H. Liu, Y. Wang, Self-generated hollow $NaTi_2(PO_4)_3$ nanocubes decorated with graphene as a large capacity and long lifetime anode for sodium-ion batteries, RSC Adv. 7 (2017) 56743-56751.

[36] A.S. Ivanova, E.M. Slavinskaya, R.V. Gulyaev, V.I. Zaikovskii, O.A. Stonkus, I.G. Danilova, L.M. Plyasova, I.A. Polukhina, A.I. Boronin, Metal-support interactions in Pt/Al_2O_3 and Pd/Al_2O_3 catalysts for CO oxidation, Appl. Catal. B-Environ. 97 (2010) 57-71.

[37] J. Lin, L. Yang, T. Wang, R. Zhou, Investigation on the structure-activity relationship of BaO promoting Pd/CeO_2-ZrO_2 catalysts for CO, HC and NO_x conversions, Phys. Chem. Chem. Phys. 19 (2017) 7844-7852.

[38] A. Sauvage, P. Massiani, M. Briend, D. Barthomeuf, F. Bozon-Verduraz, Comparison of $Pd(NH_3)_4^{2+}$ decomposition and Pd^{2+} reduction in zeolites NaY, NaX and CsX, J. Chem. Soc. Faraday Trans. 91 (1995) 3291-3297.

[39] P. Castellazzi, G. Groppi, P. Forzatti, Effect of Pt/Pd ratio on catalytic activity and redox behavior of bimetallic Pt-Pd/Al_2O_3 catalysts for CH_4 combustion, Appl. Catal. B-Environ. 95 (2010) 303-311.

[40] H. Mistry, F. Behafarid, R. Reske, A.S. Varela, P. Strasser, B.R. Cuenya, Tuning catalytic selectivity at the mesoscale via interparticle interactions, ACS Catal. 6 (2016) 1075-1080.

[41] E. Antolini, Structural parameters of supported fuel cell catalysts: The effect of particle size, inter-particle distance and metal loading on catalytic activity and fuel cell performance, Appl. Catal. B-Environ. 181 (2016) 298-313.

[42] P.G. Corradini, F.I. Pires, V.A. Paganin, J. Perez, E. Antolini, Effect of the relationship between particle size, inter-particle distance, and metal loading of carbon supported fuel cell catalysts on their catalytic activity, J. Nanopart. Res. 14 (2012).

[43] D. Roth, P. Gélin, A. Kaddouri, E. Garbowski, M. Primet, E. Tena, Oxidation behaviour and catalytic properties of Pd/Al_2O_3 catalysts in the total oxidation of methane, Catal. Today 112 (2006) 134-138.

[44] M. Chrzan, D. Chlebda, P. Jodłowski, E. Salomon, A. Kołodziej, A. Gancarczyk, M. Sitarz, J. Łojewska, Towards methane combustion mechanism on metal oxides supported catalysts: Ceria supported palladium catalysts, Topics in catalysis 62 (2019) 403-412.

[45] N. Sadokhina, G. Smedler, U. Nylén, M. Olofsson, L. Olsson, The influence of gas composition on Pd-based catalyst activity in methane oxidation-inhibition and promotion by NO, Appl. Catal. B-Environ. 200 (2017) 351-360.

[46] R.F. Hicks, H. Qi, M.L. Young, R.G. Lee, Effect of catalyst structure on methane oxidation over palladium on alumina, J. Catal. 122 (1990) 295-306.

[47] C.A. Müller, M. Maciejewski, R.A. Koeppel, A. Baiker, Combustion of methane over palladium/zirconia: effect of Pd-particle size and role of lattice oxygen, Catal. Today 47 (1999) 247-252.

[48] L.S. Escandón, S. Ordoñez, A. Vega, F.V. Díez, Oxidation of methane over palladium catalysts: Effect of the support, Chemosphere 58 (2005) 9-17.

[49] A.W. Petrov, D. Ferri, F. Krumeich, M. Nachtegaal, J.A. Van Bokhoven, O. Kröcher, Stable complete methane oxidation over palladium based zeolite catalysts, Nat. Commun. 9 (2018).

[50] K. Persson, L.D. Pfefferle, W. Schwartz, A. Ersson, S.G. Järås, Stability of palladium-based catalysts during catalytic combustion of methane: The Influence of Water, Appl. Catal. B-Environ. 47 (2007) 242-250.

[51] P. Gélin, M. Primet, Complete oxidation of methane at low temperature over noble metal based catalysts: a review, Appl. Catal. B-Environ. 39 (2002) 1-37.

[52] R. Kikuchi, S. Maeda, K. Sasaki, S. Wennerström, K. Eguchi, Low-temperature methane oxidation over oxide-supported Pd catalysts: Inhibitory effect of water vapor, Appl. Catal. A-Gen. 232 (2002) 23-28.

[53] S. Eriksson, M. Boutonnet, S. Järås, Catalytic combustion of methane in steam and carbon dioxide-diluted reaction mixtures. Appl. Catal. A-Gen. 312 (2006) 95-101.

[54] W.R. Schwartz, D. Ciuparu, L.D. Pfefferle, Combustion of methane over palladium-based catalysts: Catalytic deactivation and role of the support, J. Phys. Chem. C. 116 (2012) 8587-8593.

CAPTIONS FOR TABLES AND FIGURES

Table 1 Textural and structural properties of HAP and Pd/HAP samples calcined at different

1

Samples	BET data			XRD data				
	S_{BET}, $m^2\ g^{-1}$	Pore volume [(a)], $cm^3\ g^{-1}$	Mean pore size[(b)], nm	HAP lattice parameters[(c)]			d_{HAP}[(d)], nm	X_c[(e)], %
				a, Å	c, Å	V, $Å^3$		
HAP-773	55	0.40	27.8	9.4123 (± 0.005)	6.8810 (± 0.0002)	527.9	46	66.7
HAP-873	30	0.41	42.4	9.4159 (± 0.004)	6.8820 (± 0.0001)	528.4	49	72.7
HAP-973	23	0.33	51.8	9.4181 (± 0.004)	6.8830 (± 0.0001)	528.7	54	79.1
HAP-1073	13	0.28	42.1	9.4208 (± 0.003)	6.8820 (± 0.0001)	529.0	68	92.0
Pd/HAP-773	54	0.35	26.5	9.4127 (±0.006)	6.8794 (±0.0002)	527.8	43	58.7
Pd/HAP-873	41	0.29	29.9	9.4189 (±0.005)	6.8826 (±0.0002)	528.8	44	62.7
Pd/HAP-973	27	0.18	33.5	9.4242 (±0.007)	6.8842 (±0.0004)	529.5	47	72.1
Pd/HAP-1073	18	0.11	36.8	9.4298 (±0.005)	6.8828 (±0.0002)	530.0	57	85.2

(a) Pore volume as determined by application of BJH method.
(b) Mean pore diameter as determined by application of BJH method.
(c) Estimated through a full XRD profile refinement.
(d) Hydroxyapatite crystallite size estimated using Scherrer's equation.
(e) Degree of crystallinity of the hydroxyapatite.

Table 1

Samples	Pd^{o}	Pd^{2+}	O 1s			Ca	P	Ca/P	Pd/P	O/P	C/P
	BE, eV	BE, eV	BE, eV	BE, eV	BE, eV	BE, eV	BE, eV				
HAP-773	-	-	530.9 (87.4)	532.3 (12.6)	-	347.0	133.1	1.50	-	4.6	1.01
Pd/HAP-773	335.1 (12.4)	336.5 (87.6)	530.8 (94.2)	532.5 (5.4)	533.9 (0.4)	346.9	133.0	1.42	0.008	4.5	0.92
Pd/HAP-873	335.1 (7.8)	336.8 (92.2)	531.1 (93.7)	532.7 (6.3)	-	347.2	133.3	1.43	0.007	4.3	0.85
Pd/HAP-973	335.2 (1.6)	336.6 (98.4)	531 (93.4)	532.2 (3.2)	533.1 (3.4)	347.0	133.1	1.46	0.007	4.5	1.12
Pd/HAP-1073	335.5 (2.3)	336.8 (97.7)	531.1 (90)	532.4 (7.4)	533.3 (2.7)	347.2	133.4	1.44	0.007	4.5	1.03

* Data in brackets correspond to the relative contribution of the species (%).

Table 2

Catalyst	H_2-TPR						CH_4-TPR		
	Peak α[(a)], $\mu mol_{H2}\ g^{-1}$	Peak β[(a)], $\mu mol_{H2}\ g^{-1}$	Peak γ[(a)], $\mu mol_{H2}\ g^{-1}$	Actual H_2 uptake[(b)] for T < 373 K, $\mu mol_{H2}\ g^{-1}$	H_2/Pd[(c)]	Reducible Pd species, %[(d)]	$\mu mol_{CO2}\ g^{-1}$[(e)]	CO_2/Pd[(f)]	Reducible Pd species, %[(g)]
Pd/HAP-773	39.1 (300)	-	5.1 (331)	34.1	0.73	73	2.4	0.05	20.6
Pd/HAP-873	40.1 (301)	-	4.7 (331)	35.4	0.75	75	3.3	0.07	27.9
Pd/HAP-973	45.5 (310)	-	0.9 (331)	44.6	0.95	95	4.9	0.10	41.6
Pd/HAP-1073	25.6 (308)	20.2 (329)	-	45.8	0.97	97	6.3	0.13	54.1

(a) Estimated by the integration of the reduction peaks of Fig. 4.
(b) Calculated by subtraction of the negative peak (γ).
(c) Determined as mole of consumed H_2 per mole of total palladium (excluding the high temperature peak at T > 373 K).
(d) Determined assuming the stoichiometry of the reaction: $PdO + H_2 \rightarrow Pd + H_2O$
(e) Determined by integration of the peak at 540 K (Fig. 5).
(f) Determined as mole of produced CO_2 per mole of total palladium (peak at 540 K).
(g) Determined assuming the stoichiometry of the reaction: $4PdO + CH_4 \rightarrow 4Pd + CO_2 + 2H_2O$.

Table 3

Catalyst	TEM		H_2 chemisorption		CO_2-TPD	NH_3-TPD
	d_{Pd}[(a)], nm	X_i[(c)], nm	d_{Pd}[(d)], nm	d_{Pd}[(e)], nm	$\mu mol_{CO2}\ g^{-1}$	$\mu mol_{NH3}\ g^{-1}$
Pd/HAP-773	7 (19.6)[(b)]	162	6.5 (21.4)	8.6 (16.3)	33.8[(f)]	65[(g)]
Pd/HAP-873	8 (17.2)	174	8.6 (16.2)	7.3 (19.2)	28.7	27.8
Pd/HAP-973	9.7 (14.2)	189	18.6 (7.5)	13.2 (10.6)	24.3	28.1
Pd/HAP-1073	9.9 (13.9)	159	31 (4.5)	20 (7)	24.6	5

(a) Average size of Pd particles (TEM) for the catalysts reduced at 473 K for 2h.
(b) Pd dispersion (%).
(c) Pd interparticle distance.
(d) Pd particle size as determined by H_2 chemisorption for the fresh catalysts.
(e) Pd particles size determined by H_2 chemisorption for the catalysts submitted to three heating/cooling cycles of the reaction (Fig. 12).
(f) Total amount of desorbed CO_2 as determined by CO_2-TPD (Fig. S9(a)).
(g) Total amount of desorbed NH_3 as determined by NH_3-TPD (Fig. S9(b)).

Table 4

Catalyst	Kinetic data[a]			Stability test[b] at 723 K			
	r, $\mu mol_{CH4}\ g^{-1}\ s^{-1}$ (623 K)	TOF, s^{-1} (623 K)	Ea, kJ mol^{-1}	Initial X_{CH4}, %, under dry conditions	X_{CH4}, %, before H_2O addition (25 h TOS)[c]	X_{CH4}, %, during H_2O addition (17 h TOS)[d]	X_{CH4}, %, after stopping H_2O (10 h TOS)[e]
Pd/HAP-773	0.37	0.049	84	97	83 (16.9)[f]	40 (51.8)[g]	80
Pd/HAP-873	0.48	0.053	67	88	79 (10.8)	38 (49.4)	79
Pd/HAP-973	0.35	0.071	77	80	71 (10.8)	29 (50.6)	73
Pd/HAP-1073	0.24	0.074	78	89	81 (9.6)	37 (51.8)	77

(a) Data corresponding to the third heating cycle, taken from Fig. 11.
(b) Data extracted from Fig. 13.
(c) First stability test period, under dry conditions (1%CH_4, 20%O_2 and 79% He).
(d) Second stability test period, under humid conditions (1%CH_4, 20%O_2, 10%H_2O and 69%He).
(e) Third stability test period, under dry conditions (1%CH_4, 20%O_2 and 79% He).
(f) Activity loss (%) after 25 h TOS under dry conditions.
(g) Activity loss (%) as determined after addition of water and a subsequent 17h TOS under humid conditions.

Table 5

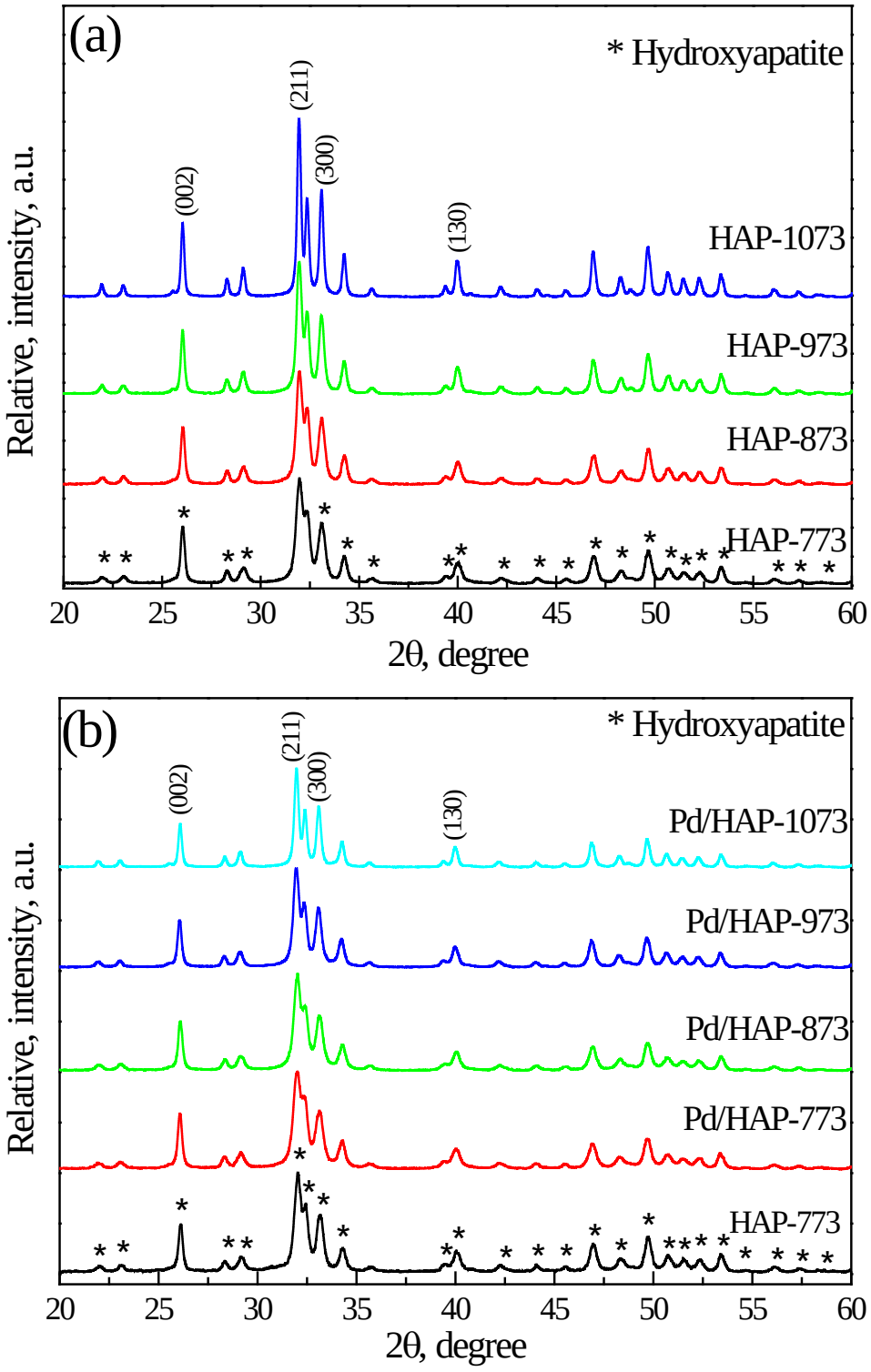
(a)
* Hydroxyapatite
(002)
(211)
(300)
(130)
HAP-1073
HAP-973
HAP-873
HAP-773
Relative, intensity, a.u.
20
25
30
35
40
45
50
55
60
2θ, degree
(b)
* Hydroxyapatite
(002)
(211)
(300)
(130)
Pd/HAP-1073
Pd/HAP-973
Pd/HAP-873
Pd/HAP-773
HAP-773
Relative, intensity, a.u.
20
25
30
35
40
45
50
55
60
2θ, degree

Figure 1

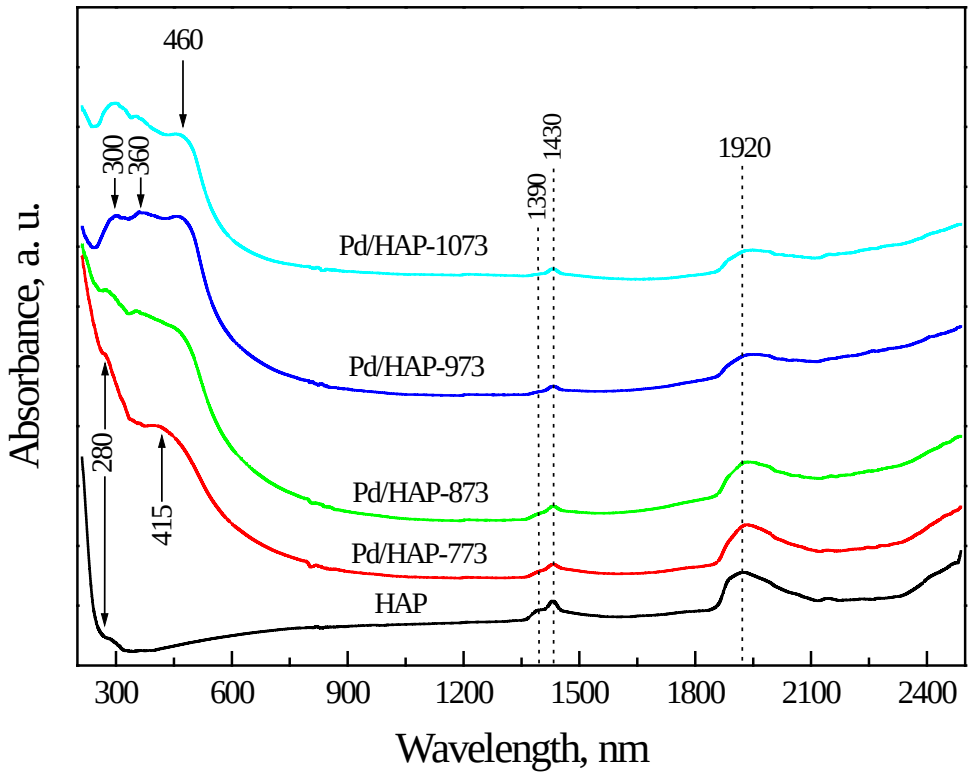
460
300
360
1390
1430
1920
Pd/HAP-1073
Pd/HAP-973
Pd/HAP-873
Pd/HAP-773
HAP
280
415
Absorbance, a. u.
300
600
900
1200
1500
1800
2100
2400
Wavelength, nm

Figure 2

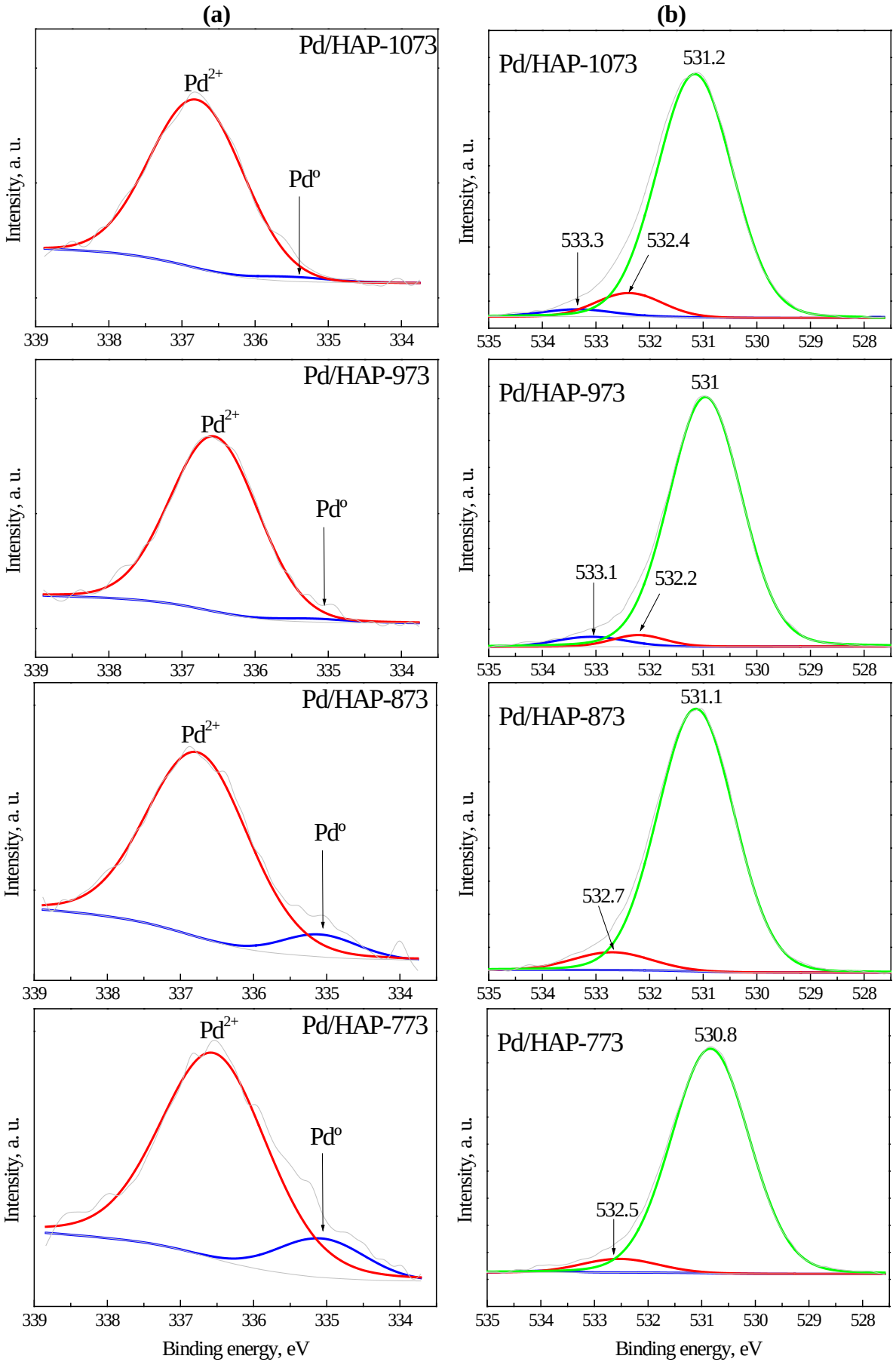
(a)
(b)
Pd/HAP-1073
Pd/HAP-973
Pd/HAP-873
Pd/HAP-773
Pd2+
Pd0
531.2
533.3
532.4
531
533.1
532.2
531.1
532.7
530.8
532.5
Intensity, a. u.
Binding energy, eV

1 Figure 3

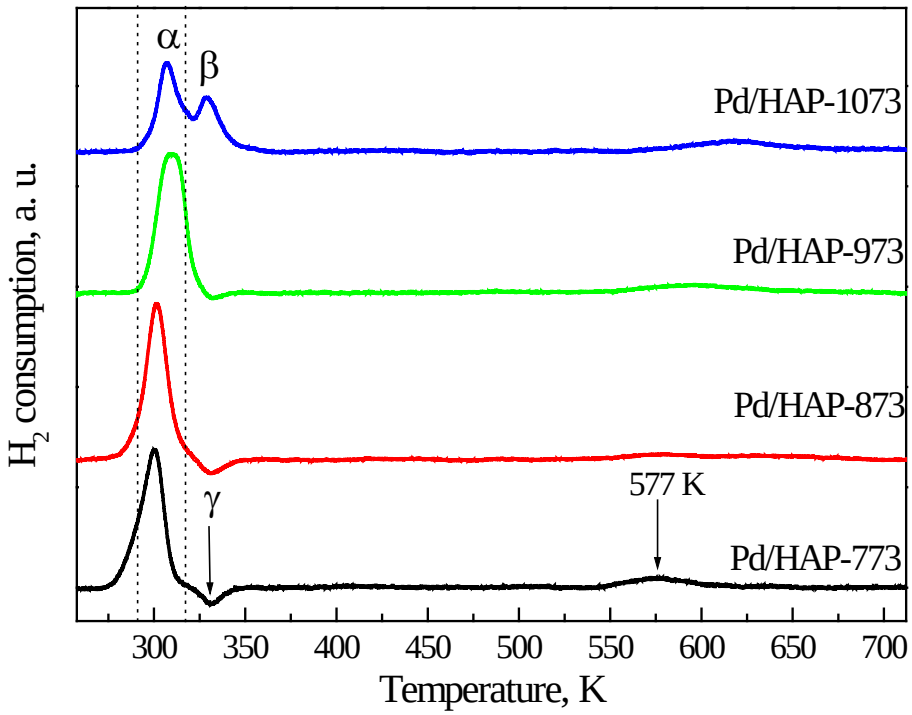
α
β
Pd/HAP-1073
Pd/HAP-973
Pd/HAP-873
γ
577 K
Pd/HAP-773
H2 consumption, a. u.
300
350
400
450
500
550
600
650
700
Temperature, K

1

2

3 Figure 4

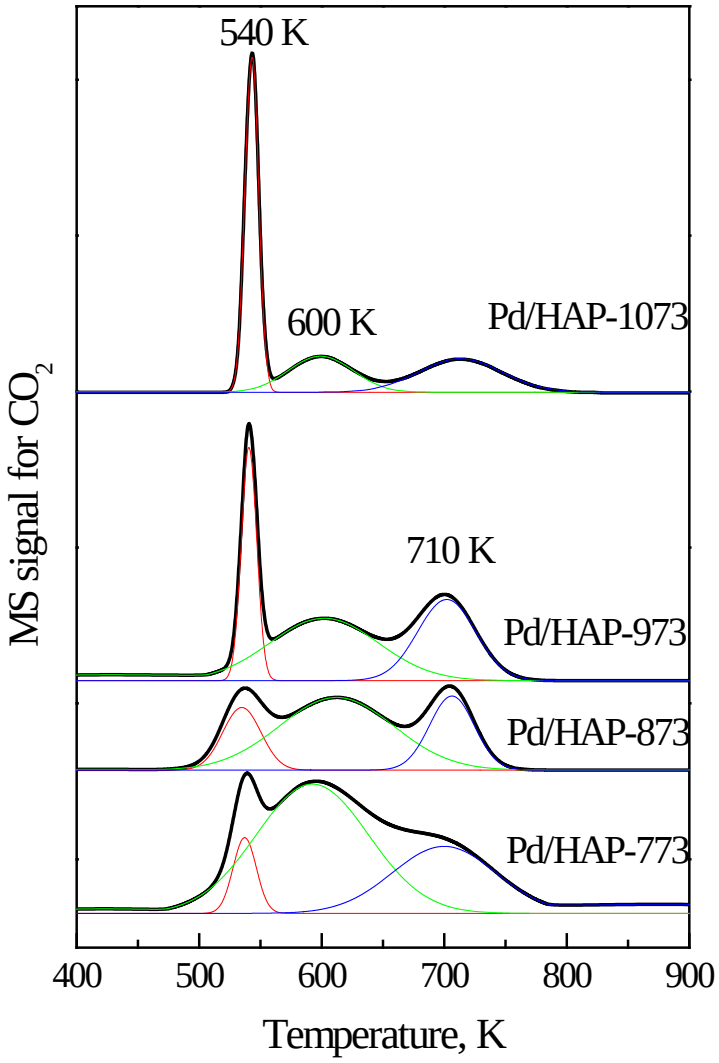
540 K
600 K
Pd/HAP-1073
710 K
Pd/HAP-973
Pd/HAP-873
Pd/HAP-773
MS signal for CO2
400
500
600
700
800
900
Temperature, K

Figure 5

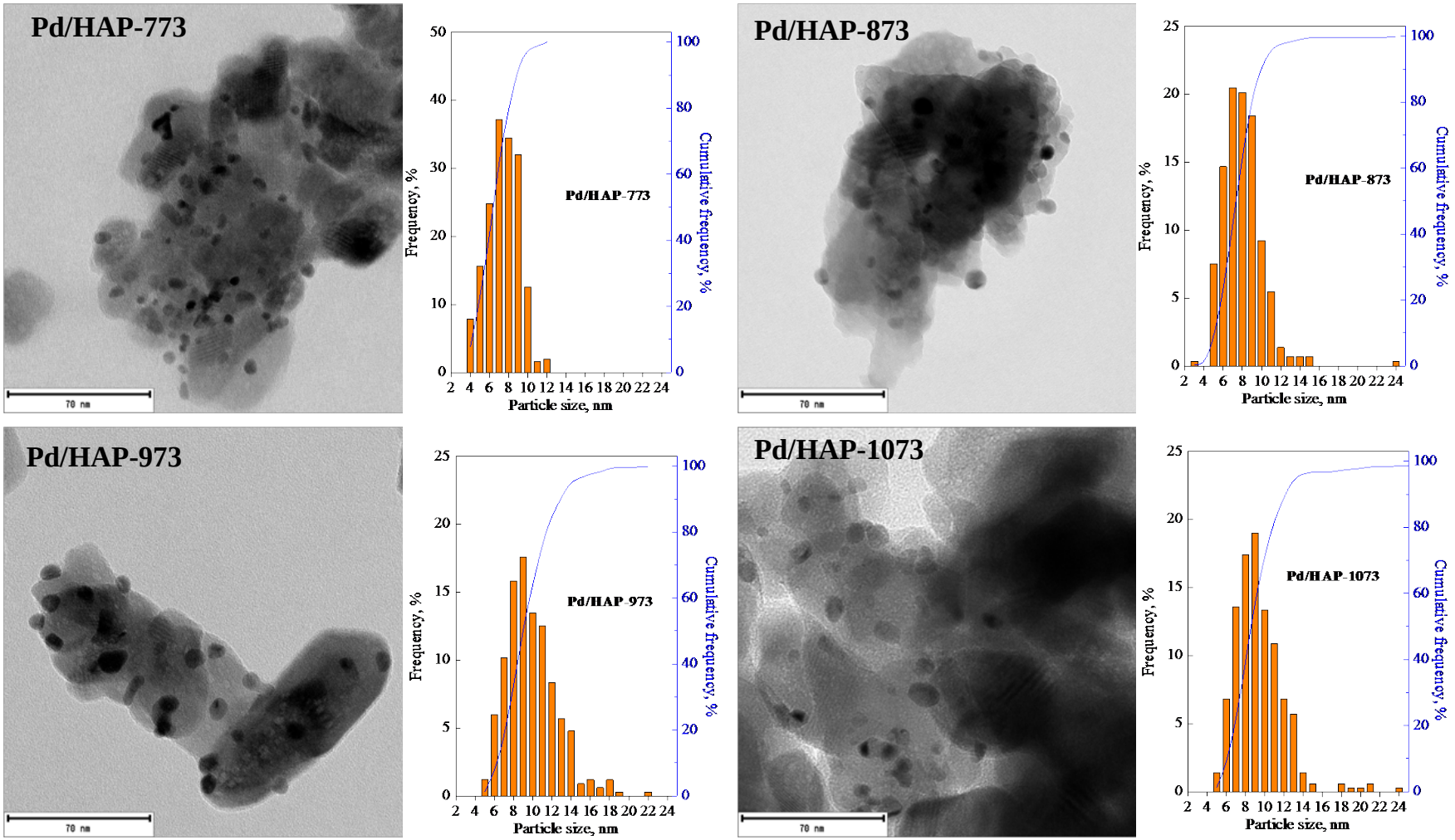
Pd/HAP-773
70 nm
Pd/HAP-773
Frequency, %
Cumulative frequency, %
Particle size, nm
Pd/HAP-873
70 nm
Pd/HAP-873
Frequency, %
Cumulative frequency, %
Particle size, nm
Pd/HAP-973
70 nm
Pd/HAP-973
Frequency, %
Cumulative frequency, %
Particle size, nm
Pd/HAP-1073
70 nm
Pd/HAP-1073
Frequency, %
Cumulative frequency, %
Particle size, nm

Figure 6

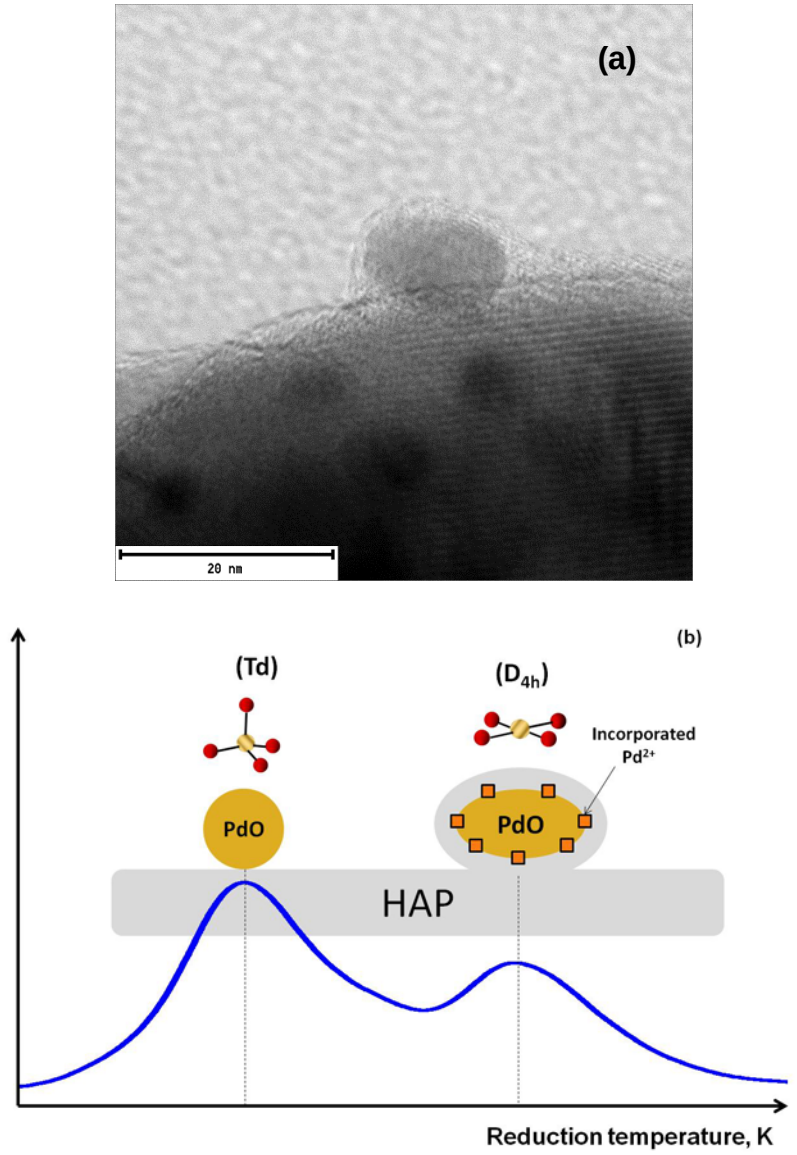
(a)
20 nm
(b)
(Td)
(D4h)
Incorporated
Pd2+
PdO
PdO
HAP
Reduction temperature, K

Figure 7

1

2

3

4

5

6

7

8

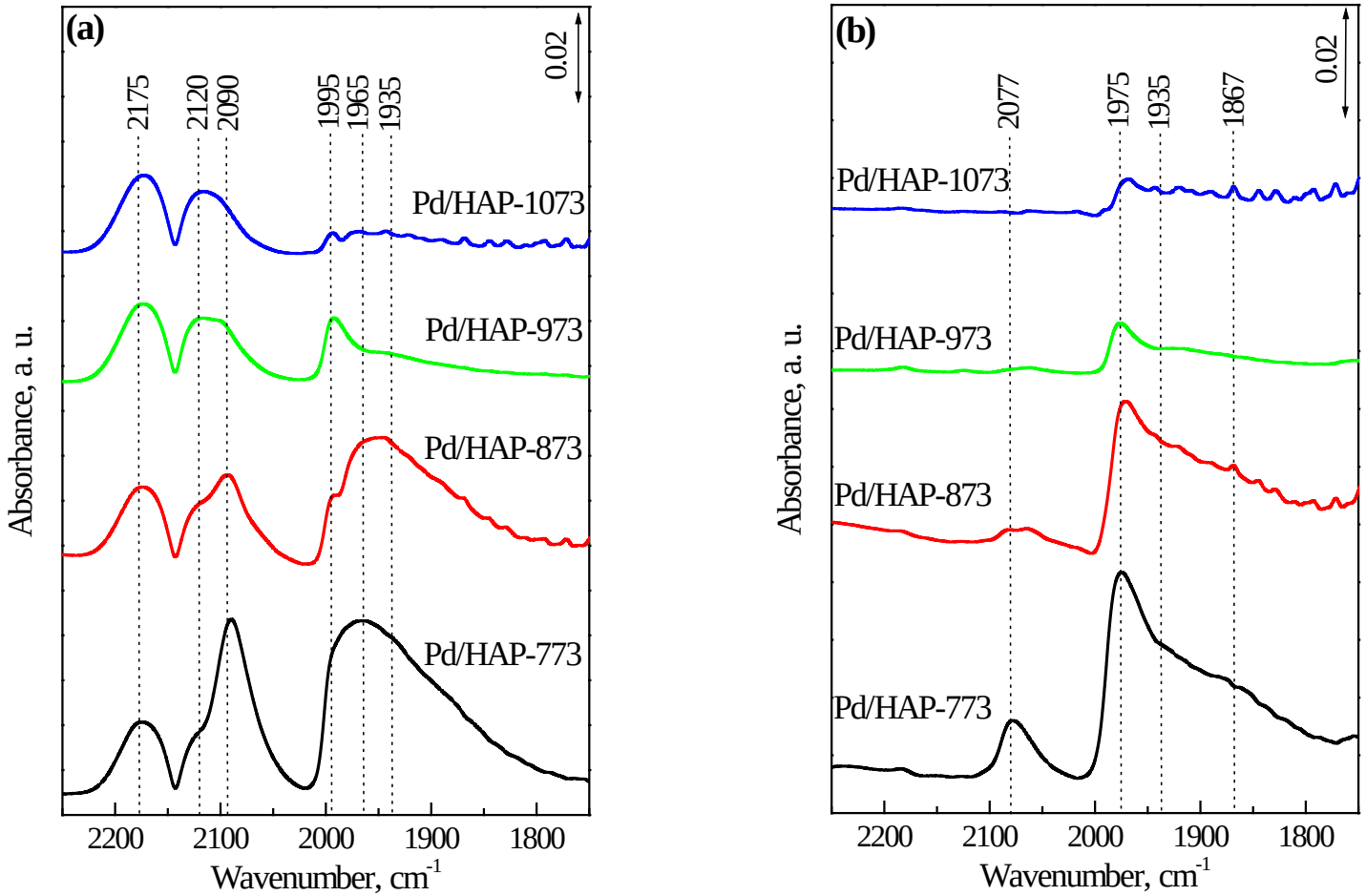
(a)
0.02
2175
2120
2090
1995
1965
1935
Pd/HAP-1073
Pd/HAP-973
Pd/HAP-873
Pd/HAP-773
Absorbance, a. u.
2200
2100
2000
1900
1800
Wavenumber, cm-1
(b)
0.02
2077
1975
1935
1867
Pd/HAP-1073
Pd/HAP-973
Pd/HAP-873
Pd/HAP-773
Absorbance, a. u.
2200
2100
2000
1900
1800
Wavenumber, cm-1

1

Figure 8

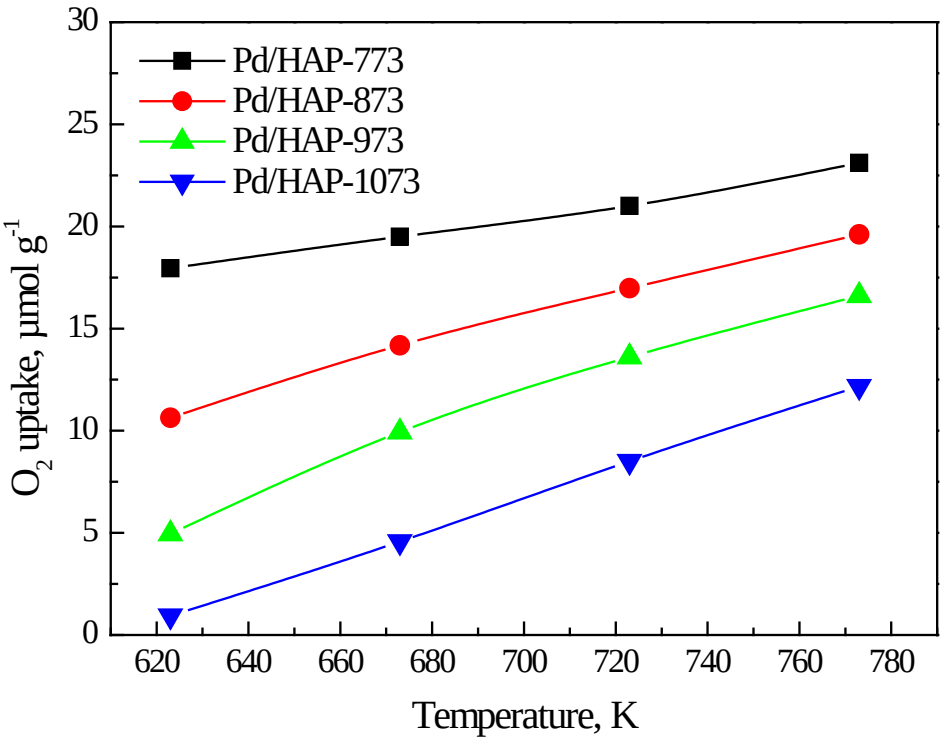
Pd/HAP-773
Pd/HAP-873
Pd/HAP-973
Pd/HAP-1073
O2 uptake, μmol g-1
Temperature, K
0
5
10
15
20
25
30
620
640
660
680
700
720
740
760
780

Figure 9

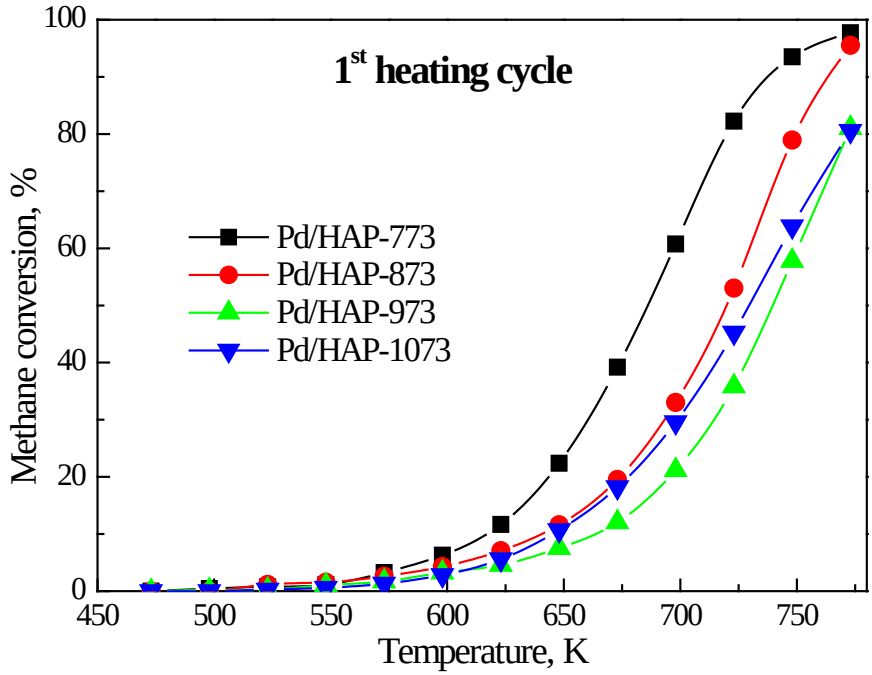
1st heating cycle
Pd/HAP-773
Pd/HAP-873
Pd/HAP-973
Pd/HAP-1073
Methane conversion, %
Temperature, K
0
20
40
60
80
100
450
500
550
600
650
700
750

Figure 10

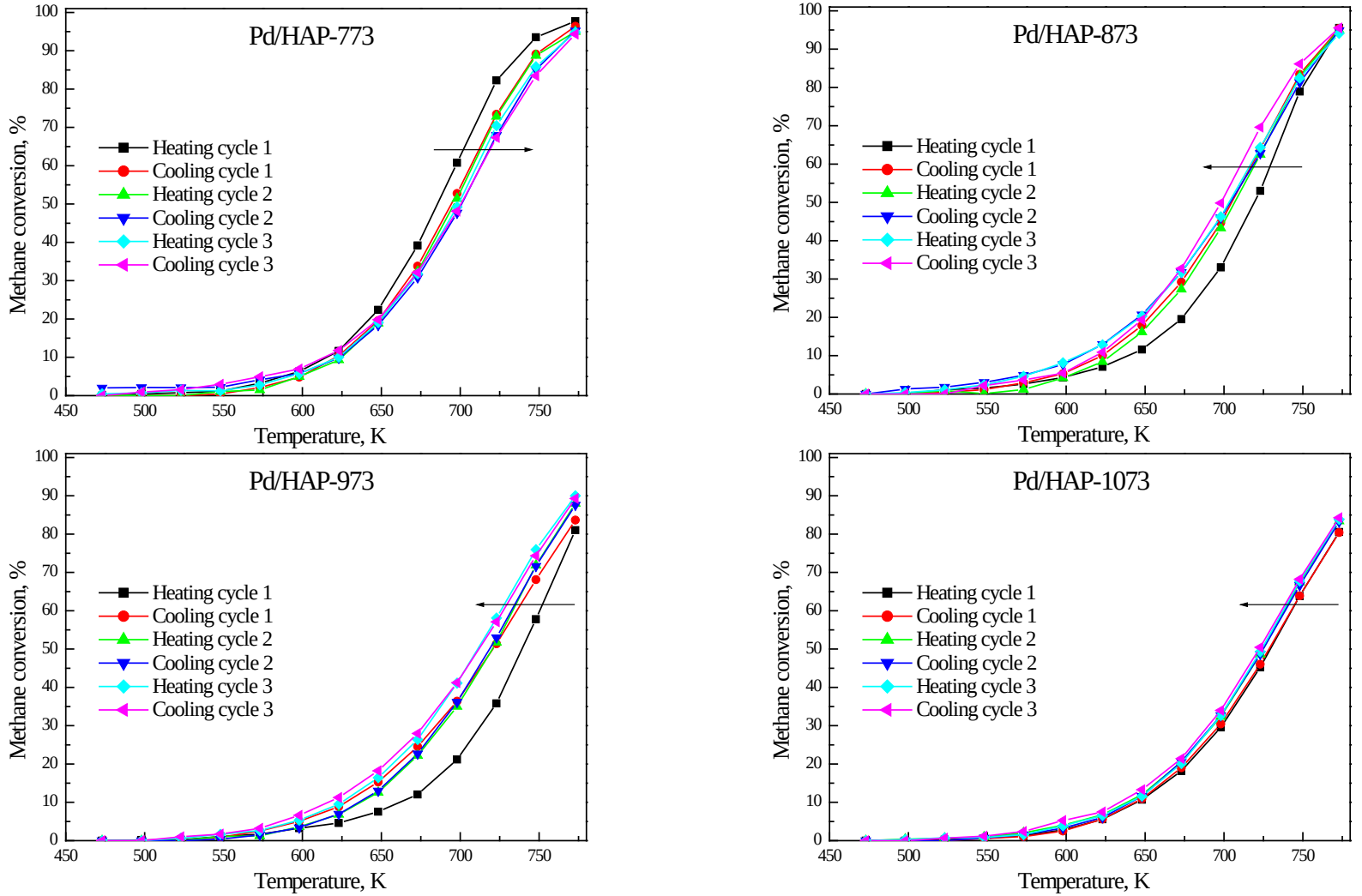
Pd/HAP-773
Pd/HAP-873
Pd/HAP-973
Pd/HAP-1073
Heating cycle 1
Cooling cycle 1
Heating cycle 2
Cooling cycle 2
Heating cycle 3
Cooling cycle 3
Methane conversion, %
Temperature, K

1 Figure 11

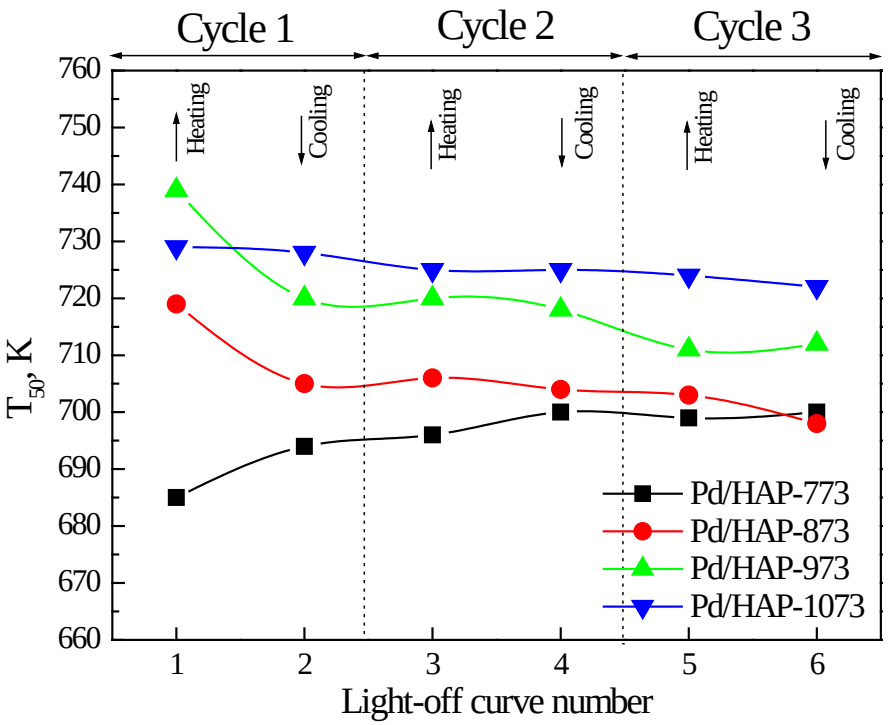
Cycle 1
Cycle 2
Cycle 3
Heating
Cooling
Heating
Cooling
Heating
Cooling
760
750
740
730
720
710
700
690
680
670
660
T50, K
1
2
3
4
5
6
Light-off curve number
Pd/HAP-773
Pd/HAP-873
Pd/HAP-973
Pd/HAP-1073

Figure 12

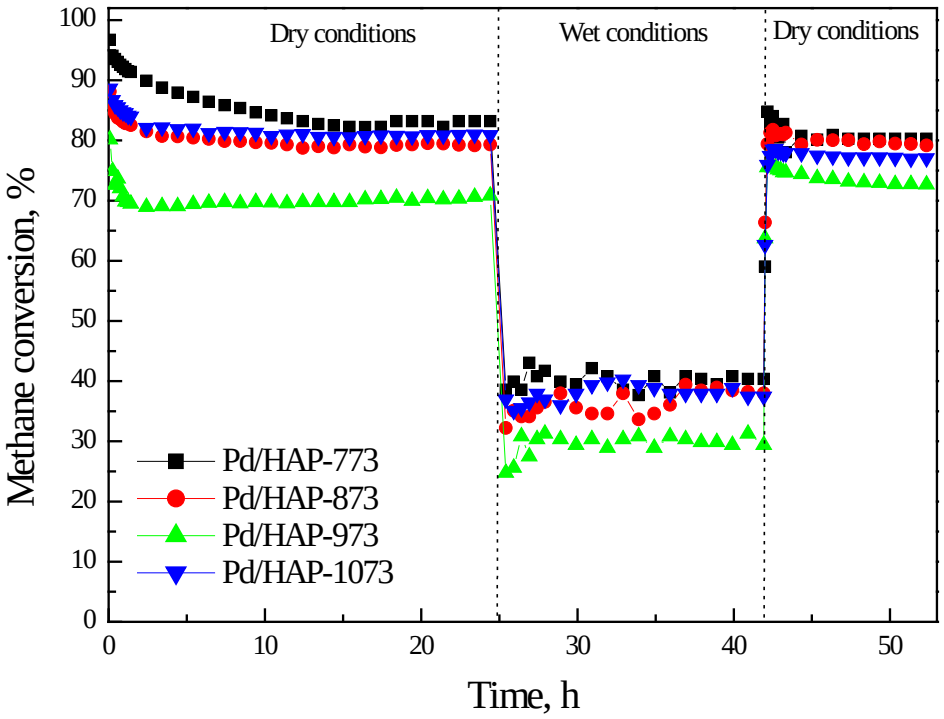
Dry conditions
Wet conditions
Dry conditions
Methane conversion, %
Time, h
Pd/HAP-773
Pd/HAP-873
Pd/HAP-973
Pd/HAP-1073
0
10
20
30
40
50
60
70
80
90
100

Figure 13

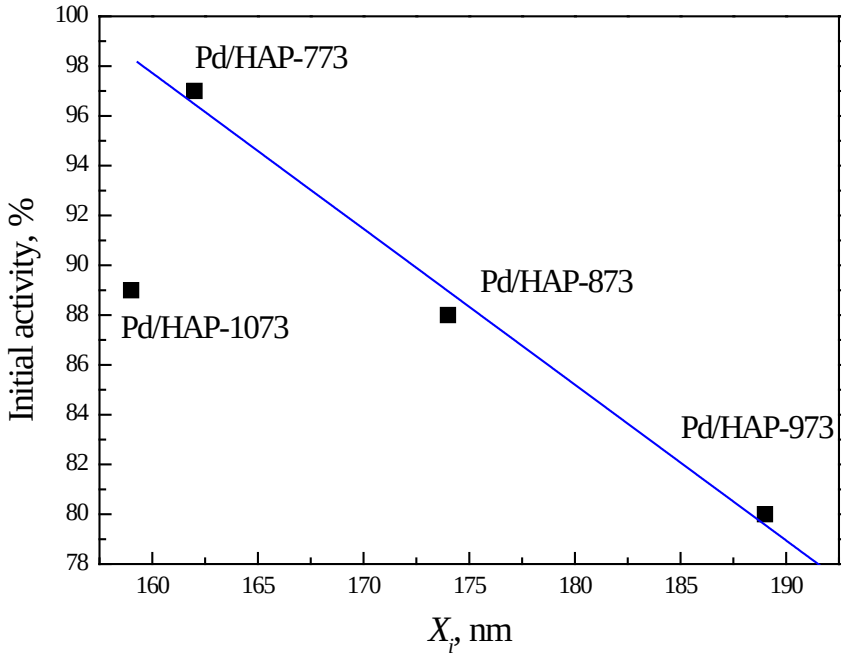
Initial activity, %
100
98
96
94
92
90
88
86
84
82
80
78
160
165
170
175
180
185
190
X_i, nm
Pd/HAP-773
Pd/HAP-873
Pd/HAP-1073
Pd/HAP-973

Figure 14

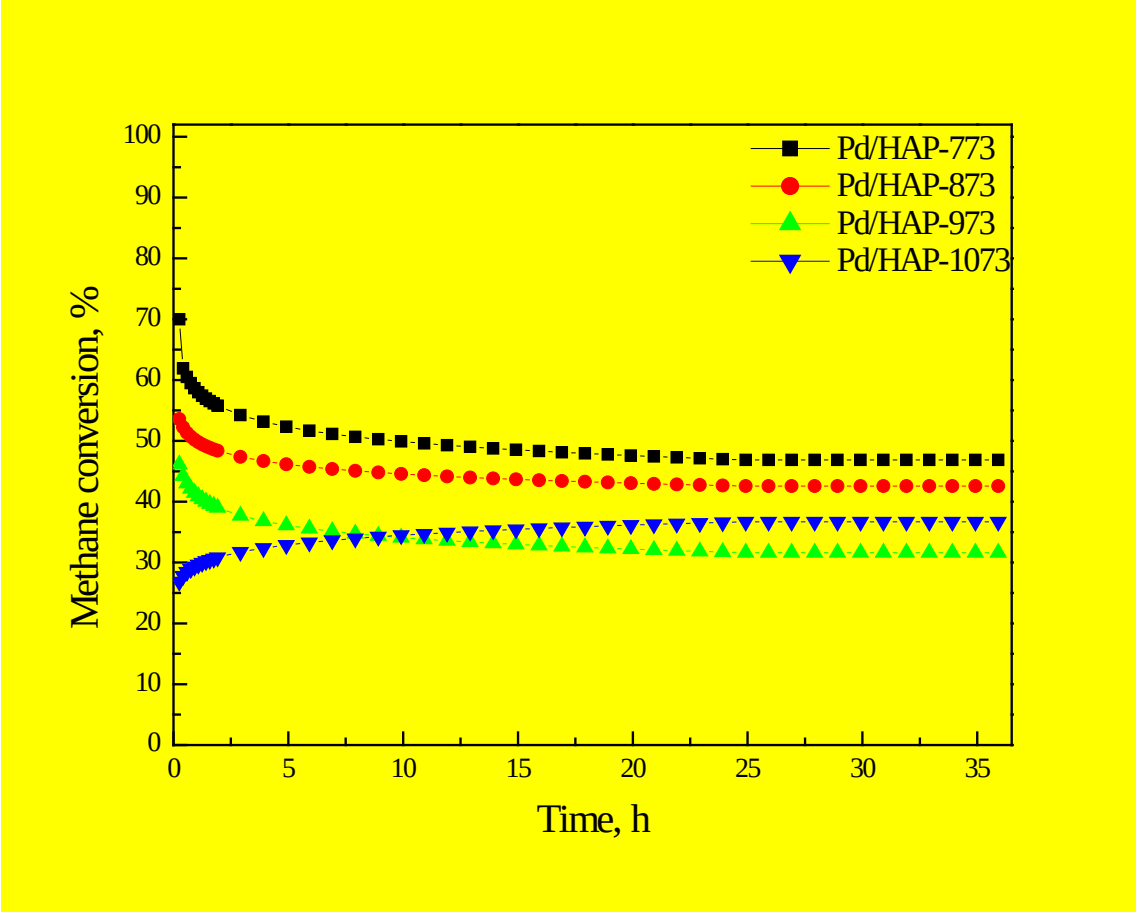
Pd/HAP-773
Pd/HAP-873
Pd/HAP-973
Pd/HAP-1073
Methane conversion, %
Time, h
0
10
20
30
40
50
60
70
80
90
100
0
5
10
15
20
25
30
35

Figure 15